THE JOURNAL OF PHYSICAL CHEMISTRY A

Article

pubs.acs.org/JPCA

Thermal Dissociation and Roaming Isomerization of Nitromethane: Experiment and Theory

Christopher J. Annesley,[†,§] John B. Randazzo,[†] Stephen J. Klippenstein,*[,†] Lawrence B. Harding,[†] Ahren W. Jasper,[‡] Yuri Georgievskii,[†] Branko Ruscic,[†] and Robert S. Tranter*[,†]

[†]Chemical Sciences and Engineering Division, Argonne National Laboratory, Argonne, Illinois 60439, United States

[‡]Combustion Research Facility, Sandia National Laboratories, Livermore, California 94551-0969, United States

Supporting Information

ABSTRACT: The thermal decomposition of nitromethane provides a classic example of the competition between roaming mediated isomerization and simple bond fission. A recent theoretical analysis suggests that as the pressure is increased from 2 to 200 Torr the product distribution undergoes a sharp transition from roaming dominated to bond-fission dominated. Laser schlieren densitometry is used to explore the variation in the effect of roaming on the density gradients for CH_3NO_2 decomposition in a shock tube for pressures of 30, 60, and 120 Torr at temperatures ranging from 1200 to 1860 K. A complementary theoretical analysis provides a novel exploration of the effects of roaming on the thermal decomposition kinetics. The analysis focuses on the roaming dynamics in a reduced dimensional space consisting of the rigid-body motions of the CH_3 and NO_2 radicals. A high-level reduced-dimensionality potential energy surface is developed from fits to large-scale multireference ab initio calculations. Rigid body trajectory simulations coupled with master equation kinetics calculations provide high-level a priori predictions for the thermal branching between roaming and dissociation. A statistical model provides a qualitative/semiquantitative interpretation of the results. Modeling efforts explore the relation between the predicted roaming branching and the observed gradients. Overall, the experiments are found to be fairly consistent with the theoretically proposed branching ratio, but they are also consistent with a no-roaming scenario and the underlying reasons are discussed. The theoretical predictions are also compared with prior theoretical predictions, with a related statistical model, and with the extant experimental data for the decomposition of CH_3NO_2, and for the reaction of CH_3 with NO_2.

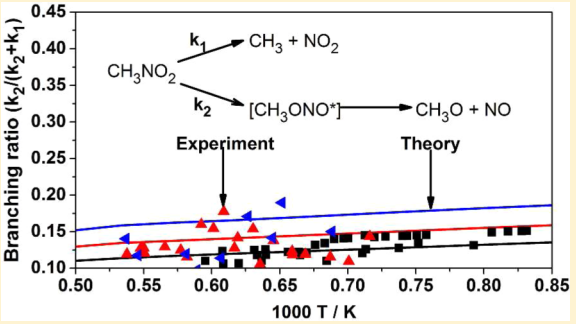

1. INTRODUCTION

Roaming reactions[1−7] are a class of unimolecular reactions that compete with bond scission reactions and generally lead to closed shell, stable species rather than reactive radical products. The kinetics of roaming reactions are important to combustion modeling because these reactions are ubiquitous,[4] and the products are typically much less reactive than those from bond scission. Consequently, the radical pool is altered, which affects simulation of many combustion phenomena such as laminar flame speeds, heat release rates, autoignition, etc. Most studies of roaming reactions in neutral molecules have focused on photodissociation experiments, beginning with the study of formaldehyde by Townsend et al.[1] The experimental literature on thermally initiated roaming reactions is still quite limited, although various recent studies have been conducted in shock tubes[8−13] and "Chen" nozzles.[14] Theoretical studies emphasizing the thermal kinetics of roaming reactions have also been presented.[3,5,10,15]

Nitromethane is an energetic material and monopropellant, and its decomposition has been studied extensively both experimentally[16−33] and theoretically.[15,16,34−42] For a long time there was some disagreement as to whether scission of the C−N bond to produce CH_3 and NO_2 was the sole decomposition reaction. This discord arose from differences found in shock tube and infrared multiphoton dissociation (IRMPD) experiments. The shock tube studies[20,21,23,26,27] span a large range of pressures and temperatures (0.15−40 atm, 1060−1490 K) and were conducted by a number of groups with different analytical techniques over more than 40 years. Consistently, only CH_3 and NO_2 were found as the primary dissociation products. However, in IRMPD experiments Wodtke et al.[25] observed formation of NO as well as CH_3 and NO_2, with the channel producing NO accounting for 40% of the nitromethane consumed. These results are also consistent with recent IRMPD experiments by Dey et al.[16] Wodtke et al. proposed that NO resulted from an isomerization with a barrier of 55.5 ±

Special Issue: 100 Years of Combustion Kinetics at Argonne: A Festschrift for Lawrence B. Harding, Joe V. Michael, and Albert F. Wagner

Received: February 15, 2015
Revised: April 1, 2015
Published: April 17, 2015

DOI: 10.1021/acs.jpca.5b01563
J. Phys. Chem. A 2015, 119, 7872−7893

1.5 kcal/mol, about 5 kcal/mol below the C−N bond dissociation energy, followed by dissociation of methyl nitrite to CH_3O + NO. Numerous theoretical studies[38,39,41,42] could not locate such a low isomerization barrier and typically found barriers about 10 kcal/mol higher than the C−N bond dissociation energy.

Notably, this difficulty was actually resolved in early multireference configuration interaction (MRCI) calculations of Saxon and Yoshimine that clearly showed a roaming mediated isomerization (RMI) path with a long-range transition state (TS) at an energy that was estimated to be 0.4 kcal/mol below CH_3 + NO_2.[40] Interestingly, this TS was "characterized as a loose combination of radical species", precisely as in subsequent roaming studies for this and related reactions. Importantly, the looseness of this TS was taken to imply that the upper bound on the IRMPD estimated barrier should be increased significantly, thereby bringing theory and observation into agreement. Saxon and Yoshimine had previously made similar observations for the corresponding rearrangement in NH_2NO_2.[43] In retrospect, these two studies appear to be the first qualitatively correct analyses of roaming transition states for neutral molecules.

Subsequent studies in 2000 by Hu et al.[39] and in 2003 by Nguyen et al.[38] failed to confirm the existence of this roaming saddle point. Ultimately, with a newfound appreciation for roaming mechanisms, Zhu et al.[37] reexplored this roaming saddle point with UCCSD(T)/CBS//UB3LYP and CASPT3//CASSCF calculations and the Saxon and Yoshimine picture was accepted as correct. Although the UCCSD(T)/CBS calculations of Zhu et al. appear to have been accepted as definitive, their focus on single-reference-based methods for both the optimization and the energy evaluation is problematic as the roaming TS is located in a region of space with large-scale multireference effects. The exploration of the global potential energy surface for the ground and excited states of CH_3NO_2 by Isegawa et al.[34] at the CASPT2//CASSCF level provides a more definitive validation of the Saxon and Yoshimine result.

In addition to the structural analysis, Zhu et al.[15,37] also used transition state theory calculations to predict branching ratios for the formation of methyl nitrite relative to C−N scission and indicated that, at the conditions of the IRMPD experiments, the roaming channel should dominate. Saxon and Yoshimine had reached similar conclusions on the basis of qualitative rate theory considerations. In contrast, at the higher pressures of the shock tube experiments the roaming channel was predicted by Zhu et al.[15,37] to be negligible, thereby effectively reconciling the differences between the products observed in thermal dissociation experiments in shock tubes and those found in IRMPD experiments. Later theoretical studies by Homayoon et al.[16,35,36] explored the roaming dynamics with quasiclassical trajectory studies, as recently reviewed by Bowman.[7] Their analyses include examination of the subsequent dynamics from the CH_3ONO isomerization products on to bimolecular products, with their predicted distribution of CH_3 + NO_2 products versus CH_3O + NO and CH_2O + HNO products correlating with the fraction that branches through the roaming mediated isomerization pathway. The product dissociation dynamics is irrelevant to the roaming mediated isomerization dynamics of interest here and so will not be considered further. Nevertheless, their predicted RMI branching provides an interesting point of comparison for the present analyses.

Zhu et al. predict strong pressure dependence in the branching ratio between 1 and 200 Torr for temperatures above 1000 K, with the mechanism changing from predominantly RMI below 2 Torr to effectively complete dissociation by C−N scission above 200 Torr. This range of conditions is accessible to laser schlieren densitometry (LS) studies behind incident shock waves, and the large difference in enthalpy of reaction between dissociation ($\Delta H_{r,298K}$ = 61.0 kcal/mol) and RMI ($\Delta H_{r,298K}$ = 2.1 kcal/mol), to which LS experiments are sensitive, should allow the branching ratio to methyl nitrite to be assessed. Consequently, in this work we present LS shock tube experiments with conditions spanning the high temperature region where a strong transition between RMI and dissociation should be observed according to Zhu et al. These experiments also encompass and extend the range of prior shock tube studies to higher temperatures and lower pressures.

This experimental study is complemented with a detailed theoretical analysis of the decomposition kinetics for CH_3NO_2, with a particular focus on the kinetic and dynamic role of the roaming mediated isomerization. The analysis also naturally leads to a treatment of the kinetics for the reverse CH_3 + NO_2 reaction. For combustion modeling purposes it is important to have quantitative rather than qualitative estimates of the roaming branching fractions. Unfortunately, although the prior theoretical studies[15,16,34−37] provide a useful qualitative description of the roaming mediated isomerization in CH_3NO_2, there are various shortcomings in the analyses that are likely to limit the accuracy of their predictions. The present theoretical study aims to remove many of these limitations via the implementation of higher level electronic structure methods and via the use of rigid body trajectories in the long-range region to more accurately explore the threshold behavior of the roaming phenomenon for this reaction.

The present theoretical analysis begins with the development of a high accuracy CASPT2-based analytic representation of the global potential energy surface (PES) for the interaction between rigid CH_3 and NO_2 radicals. The effect of fragment relaxation is incorporated through one-dimensional corrections to this rigid body PES. Rigid body trajectory (RBT) simulations on this PES then provide high-level predictions for the energy dependence of the roaming branching. A statistical framework provides a qualitative interpretation of the results. Master equation simulations incorporating the RBT predictions for the roaming branching yield predictions for the temperature and pressure dependence of the decomposition rate constants and branching fractions. These simulations incorporate stationary point properties obtained from high accuracy theoretical analyses of the thermochemistry.

A chemical model for CH_3NO_2 decomposition is used to explore the consistency between the theoretical rate predictions and the experimental observations of the shock induced density gradients. The consistency with other literature rate observations is also explored. The present theoretical predictions for the roaming branching are also compared with corresponding theoretical predictions of Zhu et al.[15] and of Homayoon et al.[35] as well as with predictions based on a statistical theory for roaming kinetics.[5] Various tests are performed to provide indications of the expected uncertainties in the present kinetic predictions.

2. EXPERIMENTAL SECTION

Density gradients behind incident shock waves were measured by laser schlieren densitometry[44] in a diaphragmless shock tube (DFST)[45] that provides excellent control over the post shock conditions. The DFST has been described previously[45] and

DOI: 10.1021/acs.jpca.5b01563
J. Phys. Chem. A 2015, 119, 7872−7893

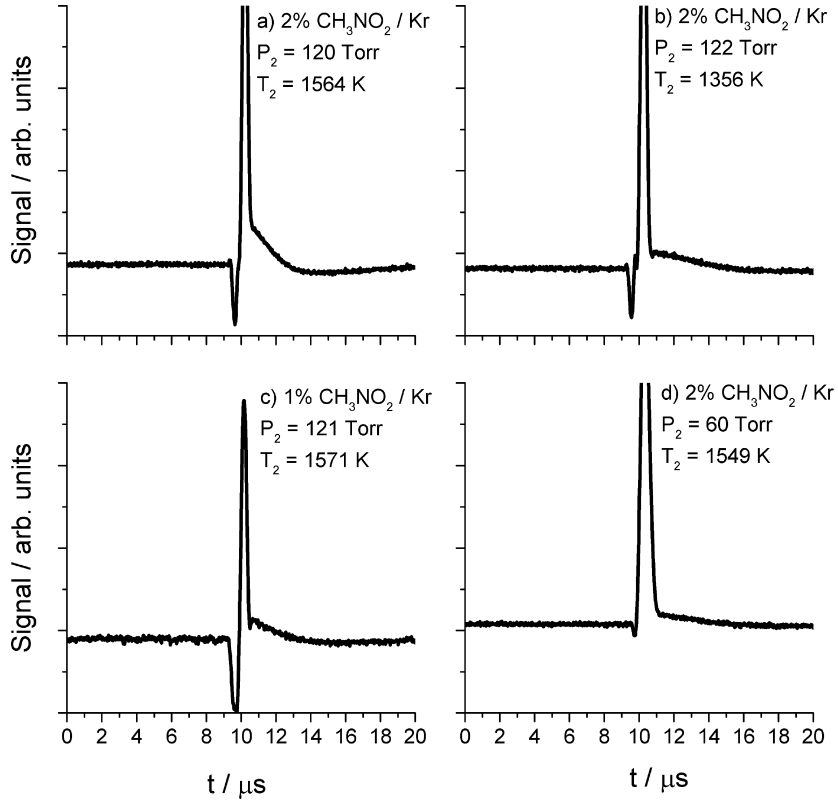

Figure 1. Raw laser schlieren signals for dissociation of nitromethane diluted in krypton.

only brief details are given here. The driver section contains a bellows-actuated fast-acting valve that replaces the more traditional diaphragm. When the valve is closed, the driver and driven sections can be filled to the desired loading pressures, and the DFST is fired by rapidly opening the valve. By varying both the driver section pressure, P_4, and the driven section pressure, P_1, the pressure behind the incident shock wave, P_2, can be constrained to narrow ranges over a wide range of temperatures. The experiments were performed with a new configuration of the driver section[46] that greatly improves the long-term reproducibility of the DFST, allowing nearly identical experiments to be performed days apart to check the consistency of the results.

A set of five pressure transducers evenly spaced (120 mm) along the side of the driven section are centered around the point where LS measurements are made. Incident shock wave velocities were obtained from the time intervals taken for the shock wave to pass between successive transducers. From these velocities and the loading conditions, the temperature and pressure behind the incident shock wave are calculated assuming frozen conditions. The uncertainty in velocity is estimated as 0.2%, corresponding to a temperature error of less than 0.5%, here amounting to 10−15 K.

The laser schlieren densitometry method has also been thoroughly described.[44,47,48] A narrow laser beam traverses the shock tube perpendicular to the direction of propagation of the shock wave. The beam is deflected by interaction with the shock front, generating the characteristic valley and peak seen in each panel of Figure 1. After the shock front passes through the laser beam, the axial density gradients in the shock heated gases, resulting from chemical reactions also deflect the beam producing the small signals to the right of the large peak, Figure 1.[44] The deflection of the laser beam is proportional to the magnitude of the density gradient, which in turn is proportional to the rate (r) and enthalpy of reaction (ΔH_r) (see appendix B in ref 44). At the start of reaction, time t_0, the only reactions contributing to the observed density gradients are dissociation and RMI of nitromethane. However, in these experiments the CH_3ONO product of RMI is not expected to be stabilized but dissociates immediately and thus as discussed later the enthaplies of reaction at t_0 are those of dissociation of nitromethane and formation of the dissociation products from CH_3ONO. As RMI is expected to be a minor channel, it should make little contribution to the initial density gradient at t_0 allowing accurate rate coefficients for dissociation to be obtained from the LS measurements at t_0. Signals at later times are composed of the sum of the density gradients from all reactions.

To then convert the raw LS signals into density gradients, the mixture molar refractivity is required. For the bath gas krypton, a molar refractivity of 6.382 $cm^3\ mol^{-1}$ was obtained from Gardiner et al.[49] The molar refractivity of nitromethane, 12.605 $cm^3\ mol^{-1}$, was calculated with the Lorenz−Lorentz equation[49] from the index of refraction (1.382) and the density (1.127 g/mL at 25 °C).[50] The normal assumption was made that the mixture molar refractivity does not vary significantly with the extent of reaction, which is an excellent approximation for dilute mixtures in krypton such as those used in the LS experiments.

The majority of the experiments reported were obtained with a new configuration of the laser schlieren setup, which will be briefly described. To obtain high quality LS profiles, it is necessary to have a stable and narrow beam, and until recently this was obtained from a Spectra Physics Model 120 helium neon (HeNe) laser (632.8 nm, 6 mW, beam diameter = 0.8 mm). This laser has been reliable but has not been produced

DOI: 10.1021/acs.jpca.5b01563
J. Phys. Chem. A 2015, 119, 7872−7893

for many years and a replacement is necessary. Recently, the HeNe laser has been replaced with a Fabrey−Perot diode laser (Newport model LQC635-08C). This laser creates a nominally circular beam (635 nm, 8 mW) of 1 mm diameter via a microlens attached to the laser exit. Initial experiments performed with the diode laser generated broad poorly shaped LS peaks, an indicator of poor beam quality, primarily due to the beam being somewhat elliptical with the long axis parallel to the direction of shock wave propagation. However, simply interposing a circular orifice of 0.6 mm diameter between the laser and the shock tube close to the entrance window of the shock tube produced very high quality signals. This circular narrow beam after the orifice resulted in a narrower peak produced from interaction of the laser and shock front compared to measurements with the original HeNe laser, which allowed meaningful chemical signal to be recovered for an additional 0.2 μs in the critical region near the start of reaction, t_0. This somewhat crude spatial filter created diffraction rings around the main beam traversing the shock tube, but deflection of the beam due to axial density gradients is too small for these to interfere with the "chemical" signal. The effective flux reaching the detector is less than from the original setup and results in a small decrease in signal/noise on a per shot basis. However, with the DFST this decrease in signal can easily be compensated for, if necessary, by signal averaging over several experiments.[46] The improved stability of the diode laser compared to the HeNe reduces artifacts in the baseline signal, which improves the quality of signals from weak density gradients.

Reagent mixtures of nitromethane dilute in krypton were prepared manometrically in a 50 L glass bulb that was previously evacuated to $<10^{-3}$ Torr. Nitromethane (Sigma-Aldrich 98.5%) was degassed prior to use. Kr was obtained from Air Gas with 99.999% purity. Mixtures were stirred with a PTFE coated magnetic stirrer and allowed to homogenize for at least an hour before use.

3. EXPERIMENTAL RESULTS AND DISCUSSION

3.1. Density Gradients. A total of 65 experiments were performed over the range 1200 < T_2 < 1860 K and nominal P_2 of 30, 60, and 120 Torr with reagent mixtures of 0.5%, 1%, 2%, and 4% nitromethane dilute in krypton. The initial and post shock temperatures, pressures, and mixture compositions for each experiment are given in Table S1 of the Supporting Information. Example plots of the raw LS signals are shown in Figure 1, and semilog plots of the absolute density gradients derived from these, in Figure 2. The small valleys and large peaks at around 10 μs in Figure 1 are due to interaction of the laser beam with the shock front[44,48] and the tailing signals to the right are from the chemical reaction. The first few microseconds of the signal are used to establish a baseline for each experiment and in all cases the "chemical" signal is initially positive and goes negative before recovering toward the baseline. This behavior is seen most clearly in Figure 2 but is also observable in the raw signals. The interaction of the shock front and laser beam obscures the start of reaction, time t_0, and this point is located with an established method[48] to an accuracy of 0.1−0.2 μs. The rate of dissociation of nitromethane is obtained from the initial density gradient, $(d\rho/dx)_0$, by extrapolating the signal back to t_0. The error in location of t_0 has a negligible effect on the derived rate coefficients. Initial estimates of $(d\rho/dx)_0$ are subsequently refined in an iterative fashion through simulation of the complete density gradient

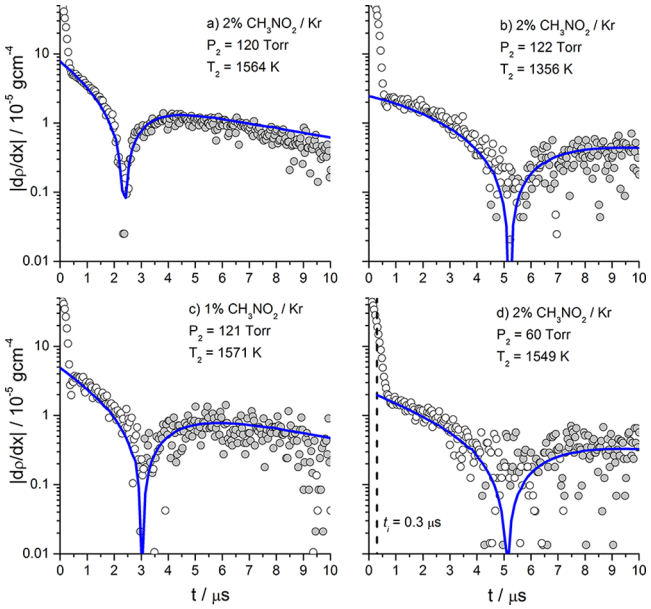

Figure 2. Semilog density gradient plots derived from the signals in Figure 1 and comparison with the simulations. Absolute values are plotted. Symbols represent experimental data and line simulations. Open and filled circles are positive and negative density gradients, respectively. The vertical dash line in (d) indicates an incubation delay.

profile with a chemical kinetic model and an in-house code for simulating chemical reactions in shock waves that incorporates the methodology of Gardiner.[49] All reactions are treated as reversible and the reverse rate coefficients are obtained via the equilibrium constant. Thermochemical properties for CH_3NO_2, CH_3O, H_2CO, CH_3, HNO, NO, NO_2, and H were taken from Active Thermochemical Tables values (cf. discussion below). For other species the thermochemical properties are from Goos et al.[51]

In Figure 2 the simulation results are compared with experiments. For the 60 and 30 Torr experiments the simulations consistently ran parallel to the underside of the experimental points and could not be brought into agreement with reasonable changes to rate coefficients, thermochemistry, or branching ratios. When this situation arises, it is typically due to incubation and small delays estimated from the method of Dove and Troe[52] were introduced for 60 Torr (~0.3 μs) and 30 Torr (~0.5 μs). The incubation delay is indicated on Figure 2d by a dashed vertical line.

3.2. Mechanism. The complete mechanism consisting of 63 reactions is available in Table S2 of the Supporting Information. The most important reactions for simulation of the experimental data are summarized in Table 1 and the reaction numbers are taken from these tables.

The reaction mechanism is composed of four main parts: (1) reactions of CH_3NO_2 and related species; (2) a submechanism for methyl radical self-reaction;[53,55] (3) a submechanism for methoxy radical reactions;[12] (4) bimolecular reactions of H, OH and CH_3 radicals. The two submechanisms were taken from prior LS studies at reaction conditions similar to those of the current work. Rate coefficients for all reactions apart from 1, 2 ,and 61 were obtained from the literature or estimated as noted in Table S2 (Supporting Information). These reactions represent, respectively, C−N scission in nitromethane, RMI, and an alternate path to recombination for the products of reaction 1.

DOI: 10.1021/acs.jpca.5b01563
J. Phys. Chem. A 2015, 119, 7872−7893

Table 1. Abbreviated Reaction Scheme for Dissociation of Nitromethane

	reaction		$\log(A)^b$	n^b	E_a/R^b	$\Delta H_{r,298K}{}^b$	ref
1[a]	$CH_3NO_2 = CH_3 + NO_2$					61.0	pw[c]
		HPL	21.718	−1.56	30964		
		120 Torr	47.978	−10.47	33808		
		60 Torr	48.075	−10.595	33927		
		30 Torr	48.016	−10.68	34307		
2	$CH_3NO_2 = CH_3O + NO$					44.8	pw[c]
		HPL	27.396	−3.91	31192		
		120 Torr	47.619	−10.67	33708		
		60 Torr	47.925	−10.82	33663		
		30 Torr	48.127	−10.95	33609		
3	$H + CH_3NO_2 = H_2 + CH_2NO_2$		2.398	3.50	2617	−3.5	24
4	$CH_3 + CH_3NO_2 = CH_4 + CH_2NO_2$		−0.260	4.00	4177	−4.3	26
5	$CH_2NO_2 = H_2CO + NO$		13.000	0.00	17325	−35.0	25, 26
6	$OH + CH_3NO_2 = H_2O + CH_2NO_2$		5.699	2.00	503	−18.2	22
8	$C_2H_6 = CH_3 + CH_3$		61.084	−13.50	55195	90.0	53, 54[d]
34	$CH_3O + M = H + H_2CO + M$		13.732	0.00	7800	20.9	12
35	$H + CH_3O = H_2 + H_2CO$		13.300	0.00	0	−83.3	12
36	$CH_3 + CH_3O = CH_4 + H_2CO$		15.875	−1.00	252	−84.1	12
55	$OH + CH_3O = H_2O + H_2CO$		13.250	0.00	0	−98.0	12
56	$HCO + OH = CO + H_2O$		14.000	0.00	0	−103.3	98
57	$CH_3OH + M = CH_3 + OH + M$		15.748	0.00	30998	92.0	12
61	$CH_3 + NO_2 = CH_3O + NO$		13.602	−0.2	0	−16.2	22
62	$HNO + M = H + NO + M$		16.079	−0.43	24899	48.3	22
63	$H + NO_2 = OH + NO$		13.945	0.00	0	−29.5	97

[a]The complete mechanism is available in Table S2 of the Supporting Information. Reaction numbering is consistent with that used in Table S2. [b]Units: kcal, mol, cm, s. $k = AT^n \exp(-E_a/RT)$ with T in K. [c]Arrhenius parameters derived from master equation results from the present work (pw). Valid for the range $500 < T < 2000$ K. [d]Reaction is pressure dependent. Arrhenius parameters are for 120 Torr.

$$CH_3NO_2 \rightarrow CH_3 + NO_2 \qquad \Delta H_{r,298K} = 61.0 \text{ kcal/mol} \tag{1}$$

$$CH_3NO_2 \rightarrow [CH_3ONO^*] \rightarrow CH_3O + NO \qquad \Delta H_{r,298K} = 44.8 \text{ kcal/mol} \tag{2}$$

$$CH_3NO_2 \rightarrow [CH_3ONO^*] \rightarrow H_2CO + HNO \qquad \Delta H_{r,298K} = 17.3 \text{ kcal/mol} \tag{2a}$$

$$CH_3 + NO_2 \rightarrow CH_3O + NO \qquad \Delta H_{r,298K} = -16.2 \text{ kcal/mol} \tag{61}$$

These reactions are intimately linked through the $CH_3\cdots NO_2$ PES and initial estimates of the rate coefficients were taken from master equation analyses that are discussed in the theory sections. For reactions that were in high temperature falloff, rate coefficients were calculated for the nominal P_2 where pressure dependent expressions were available. The majority of the reactions produce little density gradient due to small enthalpies of reaction and/or low rates of reaction and therefore the simulations exhibit little sensitivity to them. However, they are necessary for the conversion of one species to another.

Methyl nitrite is the RMI product of nitromethane and the $\Delta H_{r,298K}$ is just 2.1 kcal/mol, which would create a negligible contribution to the observed $(d\rho/dx)_0$. However, on the basis of Zhu et al.[15] and the current work, it is assumed in the mechanism that methyl nitrite is formed in an energetically excited state, CH_3ONO^* and is not stabilized but immediately dissociates. It is also assumed that CH_3O and NO are the only products from CH_3ONO^*, reaction 2. Consequently, the effective enthalpy of reaction for RMI is increased by 42.7 kcal/mol compared to CH_3ONO being first stabilized. Thus, the effective $\Delta H_{r,298K}$ for C−N bond dissociation and RMI of nitromethane only differ by 16 kcal/mol and the simulations are less sensitive than anticipated to the branching ratio. Additionally, over the range of experimental conditions, dissociation of CH_3O, reaction 34, is fast, $k_{34} \sim 4 \times 10^5$ s^{-1}, and is a major sink for methoxy radicals. The effective $\Delta H_{r,298K}$ for conversion of CH_3NO_2 to $H_2CO + NO + H$ is 4.7 kcal/mol greater than that of reaction 1, which would further suppress sensitivity to the branching ratio. However, on the time scale of an LS experiment, dissociation of CH_3O, although fast, cannot be considered instantaneous and bimolecular reactions of methoxy also influence the density gradients. Thus, the RMI path is simulated as reaction 2 rather than a combination of reactions 2 and 34.

CH_3O and NO are not the only potential products of CH_3ONO^*. It could also dissociate to HNO + H_2CO,[15] reaction 2a. This reaction has to occur, however, either by a second roaming transition state or by a tight transition state,[15] and neither is likely to compete with bond scission in highly excited methyl nitrite. Consequently, the RMI path for nitromethane is incorporated into the mechanism by only reaction 2. Any error in this assumption is negligible, as shown in Figure 3, where the results of simulations assuming excited methyl nitrite dissociates in equal proportions by reactions 2 and 2a and only by reaction 2 are compared. This lack of sensitivity to the particular route of dissociation of methyl nitrite is not surprising as ultimately reactions 2 and 2a lead to the same products, H_2CO, NO, and H. Similar comments apply to reaction 61.

DOI: 10.1021/acs.jpca.5b01563
J. Phys. Chem. A 2015, 119, 7872−7893

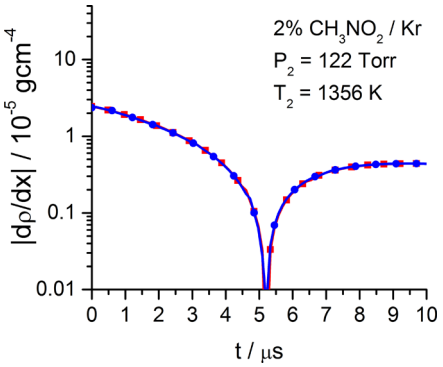

Figure 3. Comparison of simulation results for dissociation of energized CH_3ONO by reactions 2 and 2a, Table 1 or reaction 2 only. Red squares: reaction 2 only, every fourth point shown. Blue circles: reactions 2 and 2a, every fifth point shown.

The simulations shown in Figure 2 are in excellent agreement with the experiments and are representative of the complete data set. Analysis of the simulation results shows that, although the complete mechanism consists of 63 reactions, the density gradients are sensitive to only a small subset that are summarized in Table 1. The contribution of each reaction to the net (observed) density gradients was calculated and the initial positive density gradients are generated mainly by reaction 1 ($\Delta H_{r,298K}$ = 61.0 kcal/mol) with the RMI channel, reaction 2 ($\Delta H_{r,298K}$ = 44.8 kcal/mol), giving minor contributions (~10% of the net density gradient up to 1 μs). The sensitivity of the simulations to k_1 and $k_2/(k_1 + k_2)$ are shown in Figures 4 and 5, respectively. At later times,

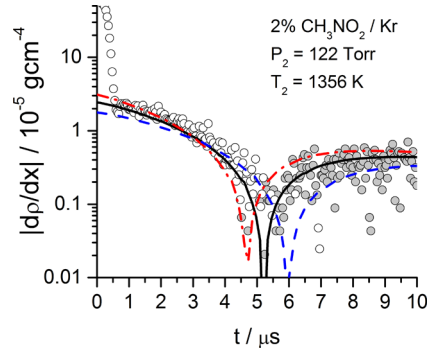

Figure 4. Sensitivity of simulations to k_1: solid black line, final model; red dash-dot line, $k_1 \times 1.3$; blue dash line, $k_1 \times 0.7$.

dissociation of CH_2NO_2, reaction 5, and CH_3O, reaction 34, are the primary sources of positive density gradients. The principal contributors to the negative density gradients are reactions 5, −8, 36, 55, 56, 61 and 63, and these start to make noticeable contributions after 1 μs for all but the highest temperature experiments where dissociation of CH_3NO_2 is very fast. Of these reactions (61), $CH_3 + NO_2 = CH_3O + NO$, and (63), $H + NO_2 = OH + NO$, are the main source of negative density gradients with the others making smaller contributions of similar magnitudes. Reaction 61 is exothermic by only 16.2 kcal/mol and its strong contribution to the net density gradient indicates it is the principle route for the consumption of methyl radicals. Furthermore, reaction 61 and not RMI, reaction 2, is the major source of methoxy radicals. Due to the high concentrations of CH_3 and NO_2 created by reaction 1 the simulations are quite sensitive to k_{61}, Figure 6. Reaction 63, H +

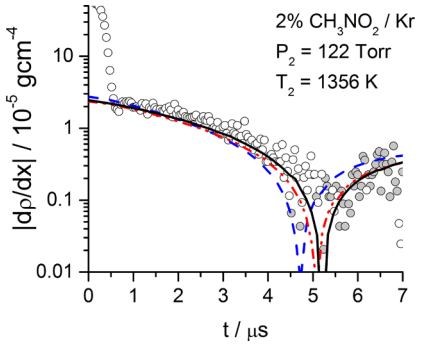

Figure 5. Sensitivity to the RMI branching ratio (BR), $k_2/(k_1 + k_2)$: black line, BR = 0.13, k_1 from Table 1; blue dash line, BR = 0.20, k_1 from Table 1; red dash line, BR = 0.2, k_1 and k_2 adjusted to keep $(d\rho/dx)_0$ the same as for the black line.

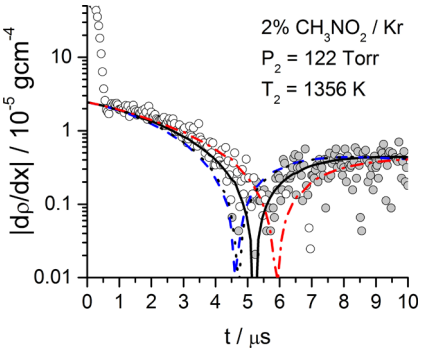

Figure 6. Sensitivity to $CH_3 + NO_2 = CH_3O + NO$, reaction 61: black solid line, final model; red dash-dot line, $k_{61} \times 0.5$; blue dash line, $k_{61} \times 2$.

$NO_2 = OH + NO$, makes similar negative contributions to the net density gradient as reaction 61. However, k_{63} is nearly an order of magnitude larger than k_{61} and the enthalpy of reaction is almost twice as large. Thus, reaction 63 actually represents a relatively minor path compared to reaction 61 and the simulations are only mildly sensitive to changes of a factor of 2 in k_{63}. Apart from reaction 63, the other reactions influencing the negative density gradients are all very exothermic, $\Delta H_{r,298K}$ = 80−100 kcal/mol, and as the density gradients for each reaction are smaller than those from reaction 61 they are minor channels. Of these reactions, (36) and (55) are additional sinks for CH_3O radicals and the high concentrations of methyl radicals generated by reaction 1 makes reaction 36 much more efficient than k_{36} (~4×10^{12} cm^3 mol^{-1} s^{-1}) would suggest.

3.3. Rate Coefficients and Branching Ratio. The rate coefficients for C−N scission in nitromethane, k_1, and branching ratios obtained from the above simulations are shown in Figures 7 and 8. The k_1 are deep into fall off and show a marked pressure dependence in accord with the current theoretical predictions, which are discussed later. The error in k_1 is difficult to assess but on the basis of experimental errors and the sensitivity of the simulations to k_1 it is estimated to be ±30%. The agreement between the present theoretical values and the present experimental results is excellent. A comparison of the present theoretical values with the experimental literature is given in section 5. The branching ratios fall in the range 0.10−0.19 with a median value of 0.13 and one standard deviation of 0.02. There is generally a slight decrease with increasing temperature, but no apparent dependence on

DOI: 10.1021/acs.jpca.5b01563
J. Phys. Chem. A 2015, 119, 7872−7893

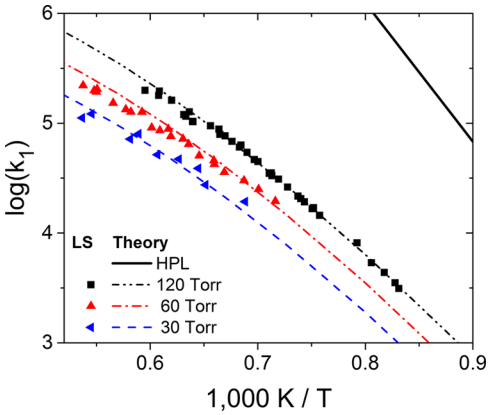

Figure 7. Arrhenius plot of k_1/s from LS experiments and theory for dissociation of CH_3NO_2 by C−N scission. Lines are current theoretical predictions with $\langle \Delta E_{down} \rangle = 320(T/300)^{0.5}$ cm^{-1}.

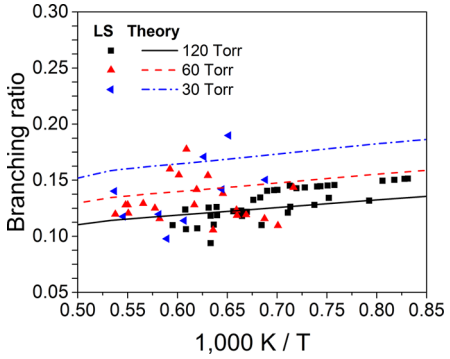

Figure 8. Comparison of branching ratios, $k_2/(k_1 + k_2)$, for dissociation of nitromethane. Lines are predictions from the current theoretical work.

pressure. The scatter in the 30 and 60 Torr data is larger than in the 120 Torr results and is mainly due to smaller density gradients in these experiments leading to greater uncertainty. Overall, there is very good agreement between the experimental results and the theoretical predictions particularly considering the challenges involved in the theoretical estimates and the experimental work. Though the experimental branching ratio shows essentially no pressure dependence, the scatter of the data is within the theoretically predicted pressure variation. This predicted pressure variation is substantially weaker than was originally predicted by Zhu et al.[15]

The above simulations were made by assuming, on the basis of literature and the current theory, that RMI would play some role in dissociation of nitromethane. It was noted earlier that the differences in enthalpies of reaction for dissociation of CH_3NO_2 by reaction 1 and RMI were much smaller than initially anticipated, which reduced the sensitivity to the effects of RMI on the density gradients at t_0. The simulations in Figure 2 represent the best fits taking into account the theoretical predictions of RMI. However, as shown in Figure 9, simulations that do not include RMI can reproduce the experimental data very well. Although only one example is shown, similar quality fits are generally obtained across the complete data set, but with a few being somewhat worse. The differences between the two models lie only in the treatment of CH_3NO_2 dissociation and, in the case without roaming, the k_1 have been increased by 15−25% to capture the early density gradients correctly. This unusual situation where two models that are so different give

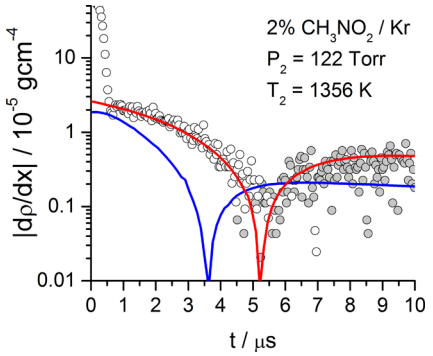

Figure 9. Comparison of two extremes for modeling the dissociation of nitromethane: red line, no RMI channel ($k_2 = 0$); blue line, only RMI ($k_1 = 0$; $k_2 = k_{1Table1}$).

such good simulations of the same LS experiments arises only because the ΔH for dissociation of nitromethane by reaction 1 differs by just 3.6 kcal/mol from formation of the ultimate products (H_2CO, NO, and H) from the RMI path and k_1 in the model without RMI is very close to $(k_1 + k_2)$ in the model with RMI. Thus, on the basis of the experiments alone it would be hard to conclude if RMI played a role in the dissociation of nitromethane. But, considering both experiment and theory, a consistent picture is obtained only when RMI is included.

Simulations have also been performed to test the upper limit of the branching ratio that can be tolerated. Across the complete data set, using branching ratios even a few percent larger than those in Figure 8 shifts the inflection point, where the net density gradient changes from positive to negative, to shorter times. This shortcoming can be corrected, but to do so requires treating k_{61} as an adjustable parameter and reducing it from the Glarborg et al. value. For instance, a mean BR of 0.16 can be accommodated if k_{61} is reduced by 10−40%, with smaller k_{61} prevailing at higher temperatures. In Figure 9 the extreme case is shown where nitromethane dissociates only by RMI. In this simulation k_2 was set equal to k_1 from Table 1 and k_{61} was from Glarborg et al. If models are generated with branching ratios between those in Table S1 (Supporting Information) and the case of only RMI, then the results fall between the two.

It was mentioned in the above discussion of the reaction mechanism that the simulations are sensitive to the value of k_{61}. Throughout the simulations k_{61} was fixed at the value of Glarborg et al.[22] The literature on reaction 61 is sparse and is summarized in Figure 10 along with the current theoretical predictions for k_{61}, which are discussed later. Clearly, there is considerable uncertainty as to the correct high temperature value of k_{61}. The current theoretical predictions agree well with the upper limit of the only high temperature experimental data, a shock tube study by Srinivasan et al.[54] However, the estimates of Glarborg et al. are a factor of ∼2.5 lower than the current theoretical predictions and are in fair agreement with the lower limit values of Srinivasan et al. With respect to the LS experiments the k_{61} from Glarborg et al. represents an upper limit (cf. Figure 6). Simulations with k_{61} from the current theory consistently become too negative almost from the start of the reaction. Given the complexity of calculating k_{61} and the challenges of directly measuring it at high temperatures, the disagreement is not severe and further study is beyond the scope of this work.

DOI: 10.1021/acs.jpca.5b01563
J. Phys. Chem. A 2015, 119, 7872−7893

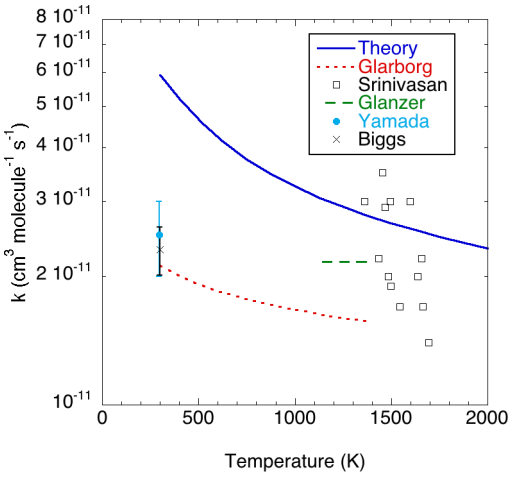

Figure 10. Plot of the RBT predictions for the high pressure limit rate coefficient for the $CH_3 + NO_2 \rightarrow CH_3ONO$ reaction together with the experimental data for k_{61}.

4. THEORETICAL METHODS

4.1. Potential Energy Surface. The stationary points on the potential energy surface relevant to the decomposition of CH_3NO_2 were characterized with a variety of ab initio electronic structure approaches. The rovibrational properties of all the stationary points were determined with ab initio, multireference, second-order perturbation theory (CASPT2). Geometry optimizations and frequency analyses were done using CASPT2 with the Dunning[56] aug-cc-pVTZ (atz) basis set. These were followed by single point CASPT2 calculations done using the larger Dunning aug-cc-pVQZ (aqz) basis set. The triple-ζ and quadruple-ζ energies were then extrapolated to the complete basis set limit (CBS). The CASPT2 calculations employ the formalism of Celani and Werner.[57]

To obtain more accurate energies for the stable species, CH_3NO_2, CH_3ONO, CH_3OON, H_2CO, and HNO, and the two relevant radical asymptotes, $CH_3 + NO_2$ and $CH_3O + NO$, CCSD(T), calculations were done using the CASPT2 geometries, again extrapolating to the CBS limit. The stationary point energies were also studied with an alternative high level approach built on CCSD(T) rovibrational analyses and extensive consideration of corrections to the CCSD(T)/CBS limit. These high level (HL) calculations provide an informative test of the more readily accessible CCSD(T)/CBS//CASPT2 method described above. In this HL approach the rovibrational analyses are performed at the CCSD(T) level with the cc-pVTZ (tz) basis set. The CBS limit is obtained from extrapolations for the aug′-cc-pVQZ (a′qz) and aug′-cc-pV5Z (a′5z) basis sets, where the prime indicates that diffuse functions are included for only the s and p orbitals in C, N, and O and the s function in H. Corrections for higher order excitations, core−valence correlation, anharmonic vibrations, and relativistic and Born−Oppenheimer effects, are obtained from CCSDT(Q)/cc-pVDZ, CCSD(T,full)/CBS(cc-pcVTZ,cc-pcVQZ), B3LYP/tz second order perturbation theory, Douglass−Kroll CI/aug-cc-pcVTZ, and HF/tz diagonal Born−Oppenheimer correction (DBOC) calculations, respectively. For a few cases difficulties were encountered with the anharmonic vibrational analyses and/or the DBOC calculations. For the former we then employed a standard correction ($-0.13n_H$) based on the number of H atoms (n_H), and for the latter we simply ignored the correction. For NO, a spin−orbit correction of −0.17 kcal/mol was also incorporated, whereas the spin−orbit correction in CH_3O was neglected due to the complication of accurately treating its coupling with Jahn−Teller effects.

For the stationary points involved in the roaming pathways, CCSD(T) calculations were found to be unreliable owing to sizable multireference character in the electronic wave functions.[40] The energies of these roaming stationary points were evaluated relative to the respective radical asymptotes using the above-mentioned CASPT2 calculations. For the $CH_3NO_2 \rightarrow CH_3ONO$ roaming path, the CASPT2 active space for the optimizations and rovibrational analyses consists of seven orbitals and ten electrons (7o,10e). The seven active orbitals include the CH_3 and NO_2 radical orbitals, three NO_2 π orbitals, and the two oxygen lone-pair orbitals. For the $CH_3ONO \rightarrow H_2CO + HNO$ roaming path, the active space consists of six orbitals and eight electrons. The six active orbitals include the CH_3O radical and oxygen lone pair orbitals and the four NO π, π^* orbitals. Because of the 4-fold near-degeneracy of the $CH_3O + NO$ asymptote, these CASSCF calculations were state averaged over the four lowest doublet states.

The $CH_3NO_2 \rightarrow CH_3ONO$ roaming saddle point is central to the present kinetic analysis. Thus, in the interest of gaining an improved understanding of the expected accuracy of the predicted energetics, we have also studied this saddle point with a variety of alternative electronic structure methods. In particular, we have estimated the energy with Davidson-corrected multireference configuration interaction (MRCI+Q) calculations employing the same (7o,10e) active space and with CASPT2 employing an (11o,14e) active space. The latter active space includes the NO σ, σ^* orbitals in addition to the above-described seven orbital active space. We have also estimated the energies from a combination of CCSD(T) evaluations for the triplet electronic state with multireference-based determinations of the singlet−triplet spin splitting. Recent studies indicate that such a spin-splitting-based analysis provides better consistency between CASPT2 and MRCI+Q results.[58,59] In each case, the CBS limit was estimated from extrapolation of calculations for the atz and aqz bases and the CASPT2-(7o,10e)/atz optimized geometries were employed in the analyses. These various approaches were also explored in studying the interaction energies for the minimum energy paths (MEP) describing the addition of CH_3 to the N and O atoms of NO_2.

The present rigid-body trajectory simulations of the dynamics in the roaming region require an analytic description of the six-dimensional interaction between rigid CH_3 and NO_2 fragments at arbitrary separations and distances, which was obtained as follows. The CASPT2/adz method was used to calculate energies on two quasirandom[60,61] grids of the five intermolecular angles and the center-of-mass distance R. A total of 12 800 energies were calculated for R = 1−20 Å, and 76 800 energies were calculated for R = 2−5 Å. The (7o,10e) active space was used in the CASPT2 calculations, and for this choice of active space, the CASSCF step converged to an inconsistent solution at some of the sampled geometries, particularly at small R. These were eliminated from the data set by comparing the difference in the CASSCF and CASPT2 energies at each sampled geometry against expected values for this quantity. The data set was further restricted to exclude energies below −15 kcal/mol relative to the $CH_3 + NO_2$ asymptote. The final data set consisted of 78 990 energies.

DOI: 10.1021/acs.jpca.5b01563
J. Phys. Chem. A 2015, 119, 7872−7893

The analytic potential energy surface was defined as a function of nine Morse variables, $y_i = \exp(-r_i/1\ \text{Å})$, where r_i for $i = 1-9$ are the three symmetry-equivalent H−N distances and the six symmetry-equivalent H−O distances. The interaction energy

$$V = \sum_{\alpha} c_\alpha B_\alpha$$

was expanded in terms of the basis functions[62]

$$B_\alpha = P[y_1^{n_1} y_2^{n_2} \cdots y_9^{n_9}]$$

where P collects symmetry-equivalent terms, and α labels the symmetrized terms. The exponents n_i were varied from 0 to 4 subject to the restriction $\Sigma_i n_i \leq 6$, resulting in 513 independent basis functions. The expansion coefficients c_α were obtained via least-squares minimization over the ab initio data, with each data point assigned an energy-dependent weight. Root-mean-square errors for energies within 1 kcal/mol of the asymptotic energy were weighted by 30, those from 1 to 15 and −1 to −15 kcal/mol were weighted by 3, those from 15 to 25 were weighted by 1, and those above 25 kcal/mol were weighted by an exponentially decreasing function of the energy. The mean unsigned error of the fitted data was 0.32 kcal/mol for the entire data set, and 0.043, 0.017, 0.012 kcal/mol for energies within 15, 3, and 1 kcal/mol of the asymptotic energy, respectively. The fitted potential is compared with the ab initio data along a two-dimensional cut in Figure 11. The analytic potential is seen to provide a very accurate representation of the ab initio data.

One-dimensional corrections were evaluated along MEPs for addition to the nitrogen and cis addition to the oxygen (trans addition to the oxygen has a significant barrier and so does not play an important role). The corrections are designed to account for limitations in the size of the active space, the size of the basis set and geometry relaxation. Geometries along the two MEPs were optimized using (11o,14e)-CASPT2/atz calculations. At these optimized geometries, single point CASPT2 calculations were done with the aqz basis set and the triple-ζ and quadruple-ζ energies were extrapolated to the CBS limit. The one-dimensional corrections then consist of the difference between the unrelaxed (7o,10e)-CASPT2/adz and the relaxed (11o,14e)-CASPT2/CBS energies along each MEP. The correction potentials along these two cuts are shown in Figure 12. A simple switching formula was used to interpolate between the two one-dimensional corrections for the CN and CO addition MEPs in the construction of a global correction potential. The difference between the C−N and C−O separations was used as a parameter in this switching.

The dependence of the MEP on the reference electronic structure method is illustrated in Figure 13 for the N and *cis*-O additions. The various methods are seen to be in reasonable accord, with the coupled-cluster plus spin-splitting-based approach bringing the CASPT2 and MRCI+Q predictions into very good agreement throughout the transition state region. Notably, a given percent variation in the MEP maps into a roughly similar percent variation in the predicted rate constant. Thus, the relatively modest variation of about 10% in the predicted MEP lends considerable confidence to the final kinetic predictions. Note that for the N addition, the correction potential has only a minor affect, decreasing the predicted rate coefficient by about 20% at low temperature, and increasing the predicted rate coefficient by up to 20% at high temperature.

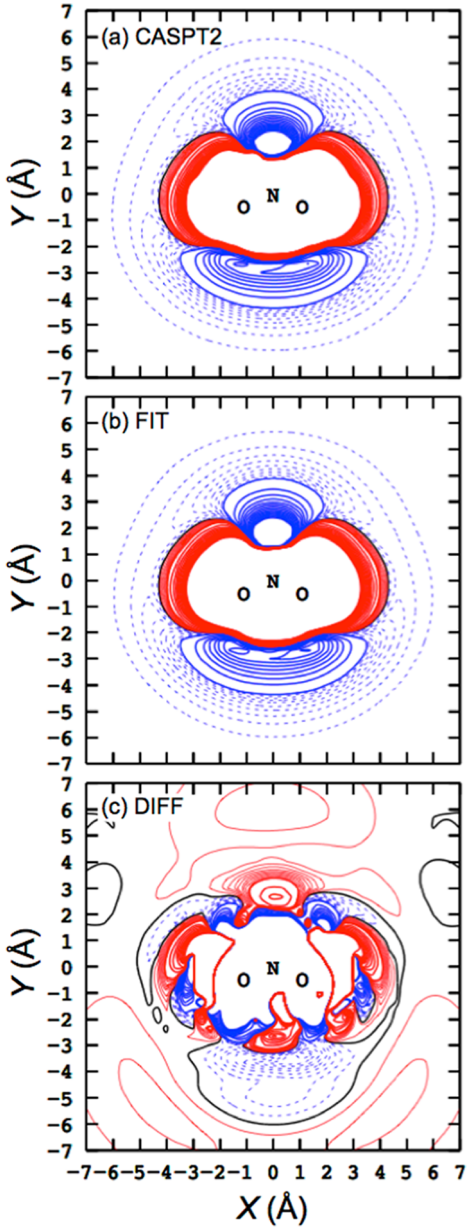

Figure 11. (a) Calculated CASPT2 and (b) fitted CH_3 + NO_2 interaction energies for geometries with the C atom in the plane of NO_2 and methyl oriented perpendicular to N−C. The contours show the asymptotic energy defining the zero of energy (black solid); 1, 2, ..., 15 kcal/mol (red solid); −1, −2, ..., −15 kcal/mol (thick blue solid); and −0.1, −0.2, ..., −0.9 (thin blue dashed). The difference potential (FIT−CASPT2) is shown in (c), where the contour scheme is similar to that of (a) and (b) except on a 10× finer scale.

The correction potential has a qualitatively similar effect on the O addition rate constant, but the increase in the predicted rate coefficient at high temperature is as large as a factor of 2. This larger affect is due to the increased magnitude of the relaxation and active space correction for the O side addition in the 2−2.4 Å region. The final rate calculations employ the correction potential based on the coupled-cluster plus spin-splitting-based PT2(11e,14o)/CBS energy relaxed MEP energy.

Various further tests of the accuracy of the final potential energy surface were performed. In particular, a separate random, but roughly uniformly dense, grid in angular space coupled with a grid in radial space that increases in density with

DOI: 10.1021/acs.jpca.5b01563
J. Phys. Chem. A 2015, 119, 7872−7893

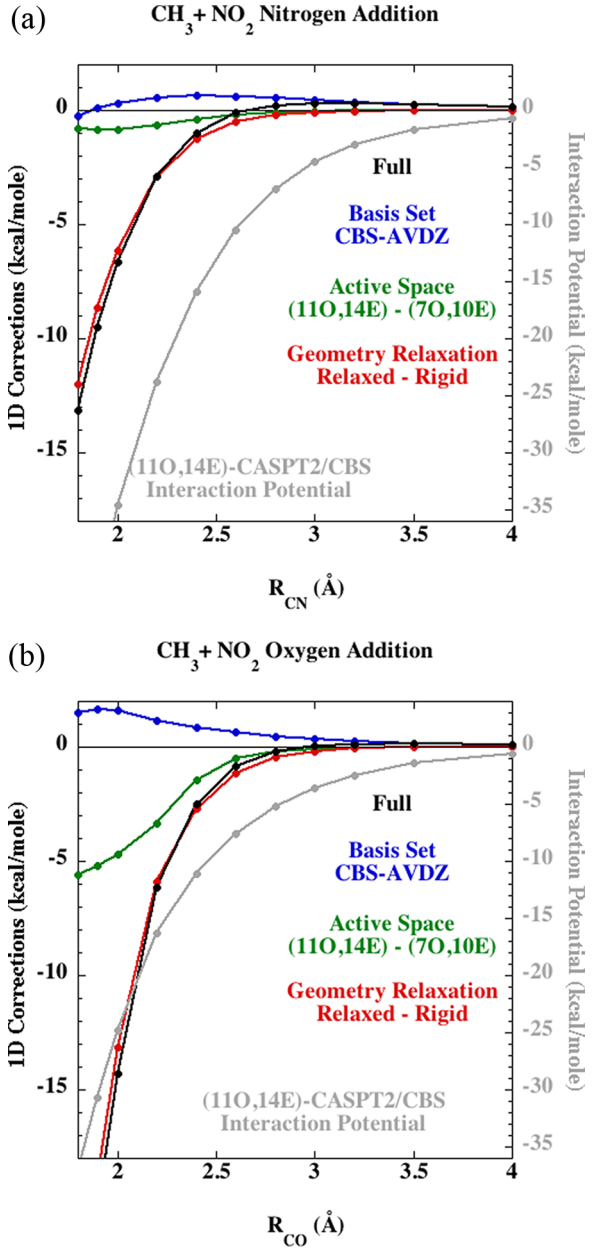

Figure 12. Interaction potentials (gray lines; right axis) and one-dimensional correction potentials (black, blue, green, and red lines; left axis) evaluated for cuts relevant to (a) nitromethane association and (b) methyl nitrite association.

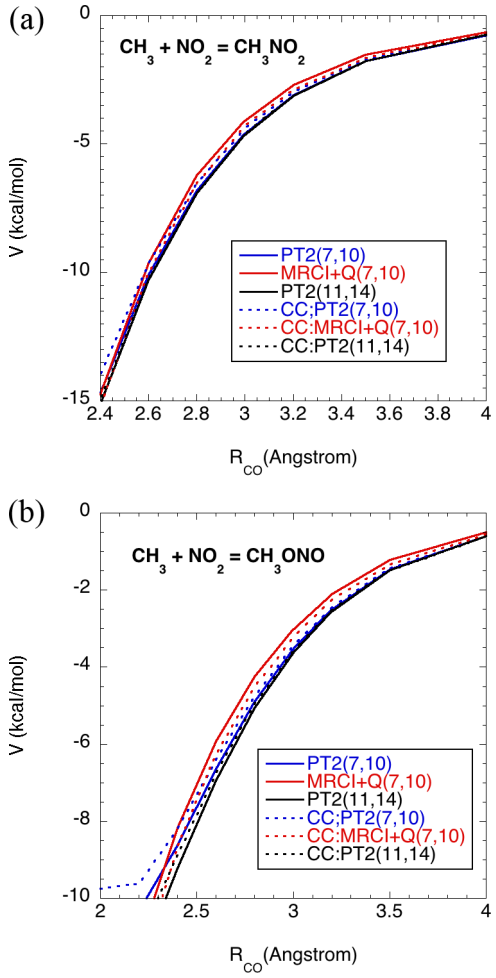

Figure 13. Interaction potentials obtained from a variety of methods for (a) nitromethane association and (b) methyl nitrite association. The CC notation denotes calculations based on CCSD(T) evaluations of the triplet states coupled with the specified evaluation of the spin splitting. The atz basis set is employed in these analyses.

decreasing separation was used to generate 3×10^5 CASPT2/adz ab initio data points. After deletion of geometries with inconsistent CASSCF orbitals, these data points were used to generate another Morse-polynomial-based analytic fit. Variable reaction coordinate transition state theory (VRC-TST)[63,64] calculations implementing the two separate analytic potential energy surfaces yielded high pressure recombination rate constants that differed by 2% or less for the addition of methyl to either the N atom or the O side of NO_2. This small difference strongly suggests that the potential is converged with respect to the number of sampling points. A third analytic potential was based on fits to MRCI+Q(7e,10o) calculations, employing a smaller set of 4×10^4 quasirandom geometries. In this case, the predicted high pressure recombination rates, after inclusion of a one-dimensional correction to the same estimated MEP energies, generally agreed to within about 10%. A final test with direct VRC-TST calculations further verified that the analytic PES employed provides an accurate reproduction of the phase space volume in the transition state region.

The second roaming pathway, $CH_3ONO \rightarrow H_2CO + HNO$, has little impact on the interpretation of the experiments described here because both CH_3O and HNO rapidly dissociate by loss of a hydrogen atom at the temperatures of these experiments. For this reason we did not attempt to calculate the branching between roaming mediated abstraction and radical dissociation for the decomposition of CH_3ONO. Nevertheless, it seemed worthwhile to explore the energetics of this pathway with CASPT2 evaluations.

The MOLPRO program package[65−69] was used for all the electronic structure calculations except the B3LYP anharmonic vibrational analyses, which were performed with G09,[70] and the DBOC calculations, which were performed with the CFOUR program package.[71] The CCSDT(Q) calculations employed the MOLPRO implementation of Kállay's MRCC code.[72]

4.2. Thermochemistry. The thermochemistry needed for benchmarking the theoretical results and interpreting the experimental observations was obtained using the Active

DOI: 10.1021/acs.jpca.5b01563
J. Phys. Chem. A 2015, 119, 7872−7893

Thermochemical Tables (ATcT) approach, which, in contrast to traditional sequential thermochemistry (A begets B, B begets C, ...), derives accurate, robust, and reliable thermochemical values by constructing, statistically analyzing, and solving a Thermochemical Network (TN). The ATcT approach has been described in more detail in earlier papers.[73−77] Tersely, the ATcT TN is constructed from relevant reaction enthalpies or Gibbs energies, bond dissociation enthalpies, constants of equilibria, adiabatic ionization energies, and electron affinities, etc. that were experimentally measured or obtained from state-of-the-art electronic structure methods. These determinations present a set of constraints that need to be satisfied by the final enthalpies of formation. After the TN is constructed, ATcT conducts an iterative analysis of internal consistency, evaluating in turn the associated uncertainty of every determination, hunting down elements of the TN that have overly optimistic uncertainties and would tend to skew the resulting enthalpies. Once internal consistency has been achieved across the whole TN, ATcT solves the resulting set of constraints and obtains the enthalpies of formation for all species simultaneously.

The current ATcT TN (ver. 1.122), is described in a companion paper in the current issue of this journal,[78] together with a selection of essential combustion-related chemical species that are relevant to the definition of sequential bond dissociation enthalpies of methane, ethane, and methanol. The last previous version[79] of the ATcT TN has been updated to incorporate, inter alia, CH_3NO_2 and CH_3ONO. The related partition functions that are used by ATcT for these two species are RRHO based, and incorporate corrections for the hindered rotors in nitromethane[80] and methyl nitrite. For the sake of consistency, the thermochemistry for key chemical species appearing in this study, including CH_3, CH_3O, H_2CO, NO_2, NO, and HNO was extracted from the current version of ATcT. ATcT outputs, in the form of tables of enthalpies of formation, heat capacities, entropies, and enthalpy increments, covering the range 100−6000 K in 50 K increments, were fitted to inverse-T polynomials using an in-house code and also to seven-term NASA polynomials using the program of McBride and Gordon.[81] The enthalpies of formation and NASA polynomials are available in Tables S3 and S4, respectively, of the Supporting Information.

4.3. Rigid Body Dynamics. Rigid-body reduced-dimensional trajectory (RBT) simulations were performed as described in refs 3 and 5 to determine the energy dependent reactive fluxes for the conversion of CH_3NO_2 into either CH_3 + NO_2 or CH_3ONO. Briefly, trajectories are initiated on approximate transition state dividing surfaces and then propagated forward and backward in time until stable products are reached. The transition state dividing surfaces consist of a union of a planar surface, providing the separation between CH_3ONO and CH_3NO_2, and spherical surfaces, representing the division between fragments and molecular complexes. Enough trajectories were run to produce estimated sampling flux errors of a few percent for the main processes. Larger uncertainties are encountered for the less probable processes at high and low energy. The simulations employ a six-dimensional analytic CASPT2-based potential energy surface together with one-dimensional correction potentials as described in the preceding section.

The reactive fluxes obtained from the RBT simulations provide the input to the master equation calculations, which are then used to determine the temperature and pressure dependence of the kinetics. The RBT simulations also automatically provide the corresponding reactive flux for the CH_3 + NO_2 association processes to form either CH_3NO_2 or CH_3ONO. Thus, we also consider the predictions for those association reactions in the results section.

For comparison purposes we have also implemented the statistical kinetic model of ref 5. The requisite transition state fluxes for this model are obtained from VRC-TST calculations. The outer transition states are assumed to have center-of-mass separations of 9 bohr and larger. For the inner transition states, the C pivot points are displaced above and below the plane of the methyl along the C_3 axis. For the addition to the N atom, the NO_2 pivot point is placed along the ONO bisector. For addition to the O side, a pair of pivot points are placed at a range of distances and angles from the O atoms. The roaming flux is evaluated as the flux through the planar dividing surface that passes through the N atom and is perpendicular to the ONO bisector. C···N separations ranging from 4 bohr to the outer transition state are assumed to contribute to the roaming flux. The requisite Monte Carlo evaluations of the partition function integrals are converged to 1%.

4.4. Thermal Kinetics. Temperature and pressure dependent phenomenological rate coefficients for the CH_3NO_2 system (including the decomposition of CH_3NO_2 to various products and the bimolecular reaction of CH_3 with NO_2) are obtained from the one-dimensional master equation (ME) employing an in-house software package.[82,83] The reactive fluxes for the roaming process and for the radical−radical recombination reactions are obtained via convolution of the transitional mode fluxes, from the rigid body reduced-dimensional trajectory simulations, with the conserved mode vibrational frequencies. The density of states for the CH_3NO_2 complex is obtained through rigid-rotor harmonic oscillator assumptions coupled with a quantum treatment of the one-dimensional hindered rotor motion. We make no attempt to determine the branching between stabilization into the CH_3ONO well and formation of the CH_3O + NO or H_2CO + HNO bimolecular products. Meaningful analyses of that branching would require careful consideration and analytic representation of the CH_3O···NO potential energy surface, which is considered beyond the scope of this effort. Homayoon et al. have considered that branching in their quasiclassical trajectory simulations.[35] Notably, those predictions suffer from the same ambiguities in the treatment of zero-point energies as do their predictions for the branching to the RMI channel, as discussed in detail below.

Lennard−Jones collision parameters were calculated using the "one-dimensional optimization" and MP2/aug′-cc-pVDZ methods, which were previously shown to predict 12/6 Lennard−Jones collision rates within ∼20% of those based on tabulated values for a variety of species.[84] For CH_3NO_2 + He, Ar, Kr, and N_2 (ε/cm^{-1}, σ/Å) = (41.7, 3.69), (197, 3.89), (242, 3.98), and (292, 3.84), respectively. Calculated Lennard−Jones parameters for CH_3ONO + M gave collision rates that differed by less than 3% from the CH_3NO_2 + M collision rates, and so the CH_3NO_2 + M results were used for both wells.

Collisional energy transfer in the master equation was described using the "exponential down" model,[85] with the temperature dependence of the range parameter α for the deactivating wing of the energy transfer represented by the expression

$$\alpha(T) = \alpha_{300}(T/300\ \mathrm{K})^n$$

In our prior studies of C_3H_8,[9] C_2H_5OH,[86] CH_3CHO,[8] CH_3OCH_3,[10] and $CH_3C(O)CH_3$[87] dissociation n was set to

DOI: 10.1021/acs.jpca.5b01563
J. Phys. Chem. A 2015, 119, 7872−7893

0.85 and α_{300} values of 100, 125, 150, 100, and 400 cm^{-1} were found to yield reasonable representations of the experimental dissociation rates. Initial attempts to fit the present data for Kr bath gas with n set to 0.85, was found to yield too large a temperature dependence. Thus, in the results section we consider fits that vary the values of both n and α_{300}. Reducing the value of n to 0.5, which is still within the range of trajectory estimates for this parameter in related systems of similar size (for example, trajectory-based values of n for linear C_4 molecules in Kr were calculated to be ~0.53[88]), yields a markedly improved fit. For α_{300} we find that the optimal value depends to some extent on the bath gas, as discussed in the theoretical results section.

5. THEORETICAL RESULTS AND DISCUSSION

5.1. Potential Energy Surface. The energies of the stationary points are shown schematically in Figure 14 and are

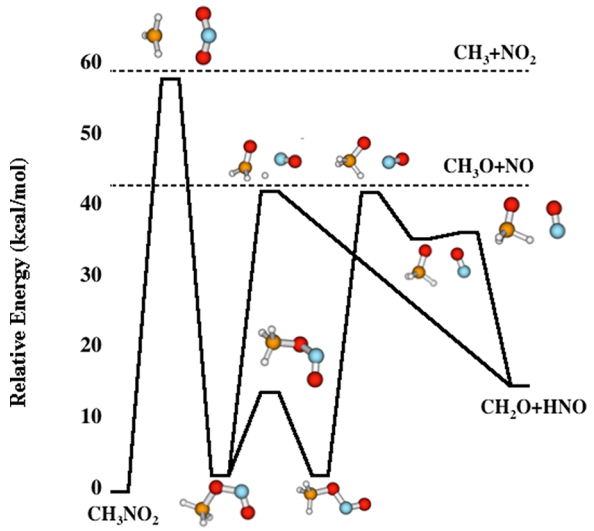

Figure 14. Schematic of the energies and geometries of the stationary points relevant to the dissociation of CH_3NO_2.

listed in Table 2 along with comparisons to three previous calculations and to the Active Thermochemical Tables (ATcT) values. The 0 and 298 K heats of formation from the ATcT analysis are reported in the Supporting Information (Tables S3 and S4 respectively) together with the NASA polynomial fits representing the temperature dependence of their thermochemical properties. The HL calculations are in excellent agreement with the ATcT values aside from CH_3O + NO, where the discrepancy is still just 0.5 kcal/mol. This modest discrepancy likely arises from the difficulty of treating the Jahn−Teller coupling and spin−orbit splitting in CH_3O, as well as irregularities in the DBOC for both CH_3O and NO.

The present CCSD(T)//CASPT2 and HL calculations are in good agreement (with a maximum discrepancy of 0.8 kcal/mol) aside from the CH_3OON minimum and the $CH_3OON \rightarrow H_2CO$ + NO saddle point. The CCSD(T)/B3LYP results of Zhu et al.[15,37] are also in reasonable agreement with a few exceptions. The B3LYP values from Homayoon et al.[35] and the CASPT2//CASSCF values from Isegawa et al.[34] show much larger discrepancies and, at least in isolation, are not kinetically useful. Note that Homayoon supplement their B3LYP-based analysis with CASSCF calculations, but due to their neglect of dispersion, CASSCF calculations tend to yield binding energies that are too small and bond distances that are too long. Our experience with treating radical−radical recombination kinetics is that CASSCF energies lead to errors in the predicted kinetics that generally exceed a factor of 2.

Our CASPT2/CBS//CASPT2/atz calculations, in agreement with the CASPT2//CASSCF calculations of Isegawa et al.,[34] find a weakly bound CH_3OON minimum along the $CH_3ONO \rightarrow H_2CO$ + HNO roaming pathway. This minimum, predicted to be bound by ~7 kcal/mol relative to CH_3O + NO, is not present in the results of either Zhu et al.[37] or Homayoon et al.[35] Though Isegawa et al.[34] do report the existence of a minimum in this region, their predicted structure and stability for it are quite different from our results, having a positive binding energy of 0.6 kcal/mol relative to CH_3O + NO and an OO distance of 2.9 Å compared to 2.0 Å in our calculations. Isegawa et al.[34] also report the existence of a second weakly bound minimum along this roaming path, labeled S_0-Q1, between CH_3ONO and CH_3OON. We do not find a minimum in this region. The differences between our calculations and those of Isegawa et al.[34] can probably be attributed to their use of CASSCF/6-31G* geometries.

The most significant difference between the four calculations relevant to the branching between dissociation and roaming in the decomposition of CH_3NO_2 is the energy and structure of the roaming saddle point in the $CH_3\cdots NO_2$ long-range region. Our CASPT2(7o,10e)/CBS//CASPT2(7o,10e)/atz calculations place this roaming saddle point at −1.1 kcal/mol relative to the radical asymptote, whereas the results from refs 34, 35, and 37 are −0.5, −0.1, and −0.6 kcal/mol, respectively. Notably, errors in the fitted potential surface from ref 35 result in the fitted zero-point-corrected, roaming, saddle point lying 0.24 kcal/mol *above* the energy of the radical asymptote. Although the energy for the roaming saddle point in our calculations is in reasonable agreement with that of both Zhu et al. and Isegawa et al., the geometries are not. Our CASPT2/atz geometry optimization leads to a CN distance of 3.04 Å at the saddle point whereas the B3LYP/6-311+G(3df,2p) calculations of Zhu et al. yield 3.48 Å and the CASSCF/6-31G* calculations from Isegawa et al.[34] yield 3.53 Å. Again, these differences are likely related to the neglect of dispersion in CASSCF calculations. Zhu et al. also report CASPT3/CASSCF results for the saddle point, which is at a remarkably low energy of −2.7 kcal/mol and again has too large a CN distance of 3.72 Å.

Due to its relevance to the present study, we have further explored the energy of the $CH_3NO_2 \rightarrow CH_3ONO$ roaming saddlepoint with a variety of additional methods, as reported in Table 3. The results reported there indicate that the CBS estimates are well converged with respect to basis set size. The MRCI+Q(7e,10o), CASPT2(7e,10o), and CASPT2(11e,14o) values range from −0.4 to −1.1 kcal/mol. The MRCI values are not expected to be accurate and are provided simply to indicate the effect of the Davidson correction, which to some extent is indicative of the uncertainty in such values. The CASPT2 predictions show little variation with active space, and yet there is a difference of 0.7 kcal/mol between these raw CASPT2 and MRCI+Q results. The coupled-cluster plus spin-splitting-based predictions show a much greater consistency, all falling within the range −0.72 ± 0.16 kcal/mol. Our best estimate is −0.78 kcal/mol, which is simply the average of the spin-splitting-based CASPT2(11e,14o) and the MRCI+Q(7e,10o) values. The 2σ uncertainty in this estimate is perhaps 0.1−0.2 kcal/mol, which arises from both the uncertainty in the underlying CCSD(T)/CBS estimate of the triplet state energy and the uncertainty in

DOI: 10.1021/acs.jpca.5b01563
J. Phys. Chem. A 2015, 119, 7872−7893

Table 2. Energies (kcal/mol) of Stationary Points Relevant to the Thermal Decomposition of CH_3NO_2[a]

stationary point	CCSD(T)//B3LYP[b]	B3LYP[c]	CASPT2//CASSCF[d]	CCSD(T)//CASPT2[e]	HL[f]	ATcT[g]
			Minima			
CH_3NO_2	−59.8 (−60.8)	−53.02	−49.6	−59.27	−59.13	−59.16 ± 0.12
cis-CH_3ONO	−58.2	−50.03	−47.7	−57.49	−57.87	−57.86 ± 0.11
trans-CH_3ONO	−57.0	−50.13	−46.5	−57.09	−57.17	−57.12 ± 0.22
CH_3OON			−11.4 [1.6][h]	−23.47 [−7.32][h]	−25.11 [−-9.61][h]	
$CH_3 + NO_2$	0	0	0	0	0	0
$CH_3O + NO$	−16.9	−17.22	−13.0	−16.15	−15.50	−16.04 ± 0.09
$H_2CO + HNO$	−43.7	−37.5	−32.4	−44.46	−43.68	−43.52 ± 0.04
$H_2CO + H + NO$					3.60	3.50 ± 0.03
			Saddle Points			
$CH_3NO_2 \rightarrow CH_3ONO$	−0.6 (−2.7)	−0.14	−0.5	−1.05		
CH_3ONO *cis* → *trans*	−46.1	−37.84	−35.2	−46.37	−45.92	
$CH_3ONO \rightarrow CH_3OON$	−17.6[i] [−0.7][h,i]		−12.4 [0.6][h]	−16.99 [−0.84][h]		
$CH_3OON \rightarrow H_2CO + HNO$			−19.6 [−6.6][h]	−23.09 [−6.94][h]	−25.09 [−9.59][h]	
$CH_3ONO \rightarrow H_2CO + HNO$[j]	−10.8 [6.1][h]	−12.07 [5.15][h]			−16.24 [−0.74][h]	

[a]All energies include zero point corrections. [b]UCCSD(T)/CBS(DZ,TZ,QZ)//UB3LYP/6-311+G(3df,2p) values from Zhu et al.[15,37] The numbers in parentheses denote CASPT3(8o,8e)/6-311+G(3df,2p)//CAS(8o,8e)/6-311+G(d) values. [c]UB3LYP/6-311++G(d,p) values from Homayoon et al.[35] The UCCSD(T)/CBS//UB3LYP/6-311+G(d,p) values from ref 35 are essentially identical to the corresponding values from Zhu et al.[15,37] [d]CASPT2(11o,14e)/6-311++G(d,p)//CAS(9o,12e)/6-31G* from Isegawa et al.[34] For comparison purposes the electronic energies from ref 34 have been adjusted by the present CASPT2(7o,10e)/atz zero point energies. [e]Present CCSD(T)/CBS(atz,aqz)//CASPT2(7o,10e)/atz or CASPT2(7o,10e)/CBS(atz,aqz)//CASPT2(7o,10e)/atz results as described in the text. [f]Present high level results from CCSD(T)/CBS(a′qz,a′5z)//CCSD(T)/cc-pVTZ calculations with corrections. [g]Active Thermochemical Tables version 1.122. [h]Numbers in brackets denote energy relative to $CH_3O + NO$. [i]$CH_3ONO \rightarrow H_2CO + NO$ roaming saddle point. [j]$CH_3ONO \rightarrow H_2CO + NO$ tight saddle point.

Table 3. Roaming Saddle Point Energy for $CH_3NO_2 \rightarrow CH_3ONO$[a]

	basis			
method	adz	atz	aqz	CBS
CASPT2(7o,10e)	−1.35	−1.21	−1.11	−1.05
CASPT2(11o,14e)	−1.30	−1.15	−1.05	−0.99
MRCI(7o,10e)	−0.29	−0.06	0.07	0.16
MRCI+Q(7o,10e)	−0.80	−0.58	−0.45	−0.36
CCSD(T);CASPT2(7o,10e)[b]	−1.17	−0.99	−0.89	−0.81
CCSD(T);CASPT2(11o,14e)[b]	−1.22	−1.04	−0.93	−0.88
CCSD(T);MRCI(7o,10e)[b]	−0.94	−0.76	−0.64	−0.56
CCSD(T);MRCI+Q(7o,10e)[b]	−1.08	−0.88	−0.76	−0.68

[a]All energies are in kcal/mol relative to $CH_3 + NO_2$, include the CASPT2(7o,10e)/atz estimated zero-point correction, and are calculated at the CASPT2(7e,10o)/atz geometries. [b]Evaluated from a CCSD(T) evaluation of the triplet state and the specified multireference-based evaluation of the singlet−triplet splitting.

the spin-splitting. Notably, the CCSDT(Q)/cc-pVDZ, core−valence, and relativistic corrections for the triplet state energy relative to $CH_3 + NO_2$ are just +0.016, −0.018, and +0.001 kcal/mol, respectively, suggesting the uncertainty in this energy is very small.

Chemical reaction rates also depend strongly on the vibrational frequencies at the saddle point. Notably, the CASPT2, B3LYP, and CASSCF methods also predict very different vibrational frequencies for the roaming saddle points, as reported in Table 4. The smaller values observed for the B3LYP and CASSCF methods correlate with expectations for the larger CN distance. For harmonic oscillator assumptions, the transition state partition function is proportional to the product of these lowest frequencies. The ratio of these products is 0.19 and 0.05 for the B3LYP/CASPT2 and CASSCF/CASPT2 comparisons, respectively. Although harmonic oscillator assumptions are not expected to be quantitatively accurate, the harmonic ratios should still be representative of the true ratios of state densities. Clearly, kinetic predictions for the flux through the roaming saddle point based on B3LYP or CASSCF potentials cannot be expected to be quantitatively accurate.

Similar differences between the CASPT2, B3LYP, and CASSCF geometries and frequencies are found for the roaming

Table 4. Lowest Vibrational Frequencies (cm^{-1}) for $CH_3NO_2 \rightarrow CH_3ONO$ Roaming Saddle Point

mode	CASPT2(7o,10e)/atz	B3LYP/6-311++G(d,p)	CASSCF(11o,14e)/6-31G*	B3LYP/CASPT2[a]	CASSCF/CASPT2[a]
ν_{imag}	179i	121i	69i		
ν_1[b]	14i	18	11i		
ν_2	87	49	42	0.57	0.48
ν_3	97	54	55	0.57	0.56
ν_4	149	115	83	0.77	0.55
ν_5	155	118	84	0.76	0.54
ν_6	588	573	355	0.98	0.60

[a]Ratio of the B3LYP to CASPT2 or CASSCF to CASPT2 frequencies for the modes with real frequencies. [b]The small imaginary value obtained for this mode in the CASSCF and CASPT2 analysis is simply indicative of numerical difficulties for such low frequency modes. In effect, this methyl torsional mode is a free rotor in the roaming saddle point.

DOI: 10.1021/acs.jpca.5b01563
J. Phys. Chem. A 2015, 119, 7872−7893

saddle point in the $CH_3O\cdots NO$ region of the potential energy surface. Indeed, as described above, for this case even the topography of the surface is method dependent.

The topography of the roaming process in the $CH_3\cdots NO_2$ region is illustrated in Figure 15 where the interaction potential

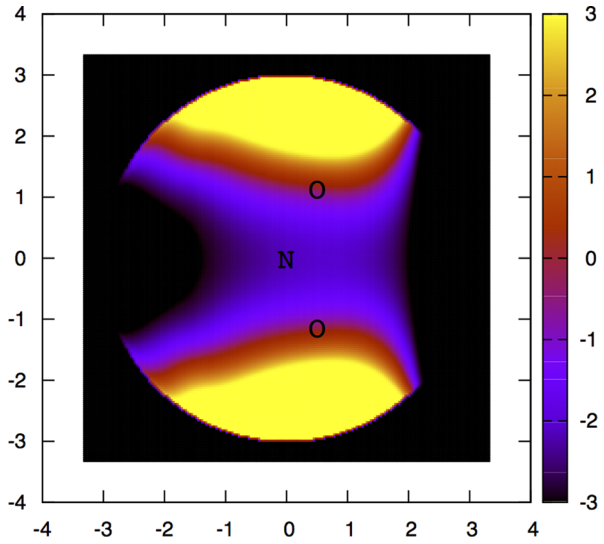

Figure 15. Plot of the (7o,10e)-CASPT2/adz interaction potential between CH_3 and NO_2 at a fixed CN distance of 3.0 Å (approximately the separation at the roaming saddle point). The potential values for each orientation are projected onto the plane of the plot. Red to yellow colors represent increasingly repulsive interactions and purple to black represent increasingly attractive interactions, as noted in the color scale on the right. The geometries of the CH_3 and NO_2 fragments are fixed. The orientation of the CH_3 with respect to the NO_2 is optimized.

between CH_3 and NO_2 is illustrated for a fixed CN distance of 3.0 Å, which corresponds to the CN distance at the roaming saddle point. The middle left of this plot corresponds to the CH_3NO_2 minima, whereas the middle right of the plot corresponds to the CH_3ONO minimum. The minimum energy path for the roaming mediated isomerization process, $CH_3NO_2 \rightarrow CH_3ONO$, corresponds to the motion along the horizontal line from left to right. The overall dynamics involves first the partial CN bond fission to yield $CH_3\cdots NO_2$ at a CN separation of about 3 Å, followed by the roaming along the horizontal path in this plot, and then the formation of the CO bond as the CH_3 group gets pulled in to the O atom. Although there are no saddle points for the first and last stages of this process, there are still bottlenecks to both the bond fission and bond reformation processes.

A contour plot of the interaction energies on the transition state dividing surface for the roaming motion is provided in Figure 16. The plane of the plot is perpendicular to the horizontal line of Figure 15, and passes through the N atom, which is roughly the location of the roaming saddle point. This plot shows that the preferred roaming path proceeds directly over the N atom at a CN separation of 3 Å. However, there is a considerable range of orientations and separations for which the roaming path lies below the asymptotic energy of CH_3 + NO_2. Indeed, a purely attractive roaming path exists even in the plane of the NO_2 fragment. A proper evaluation of the roaming flux should consider the full range of these paths, as in the present RBT and statistical theory calculations. Note that the roaming paths do not extend to short separations, which

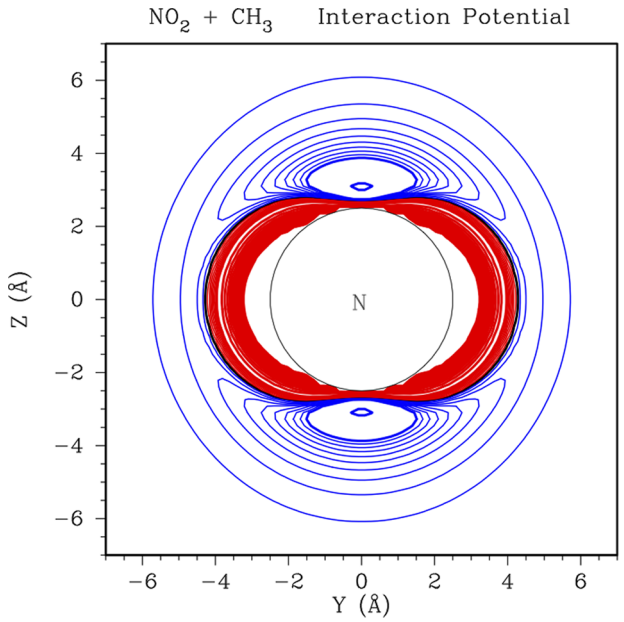

Figure 16. Plot of the (7o,10e)-CASPT2/adz interaction potential for the motion of CH_3 relative to NO_2 in the roaming dividing surface separating CH_3NO_2 from CH_3ONO. The plane of the plot contains the nitrogen atom and is perpendicular to the ONO bisector. The methyl H's are oriented as they are in the roaming saddle point. The blue lines denote attractive contours, and the red lines denote repulsive. The first 10 lines have a spacing of 0.1 kcal/mol, and the thicker lines have a spacing of 1 kcal/mol.

provides strong motivation for the present rigid-body reduced-dimensionality treatments.

5.2. Microcanonical Kinetics. A statistical framework for interpreting and evaluating the kinetics of roaming has been developed from the consideration of the multiple bottlenecks correlating with partial bond fissions, roaming, and full separation to bimolecular products.[5] In essence, one considers the long-range roaming region to consist of a number of effective intermediates and then solves for the kinetics of formation, isomerization, and decay of these intermediates. This framework provides a useful conceptual picture of the roaming dynamics and kinetics. It is also semiquantitative in its predictions, with deviations between it and the RBT results providing interesting indications of a dynamical preference for roaming at low energies and a dynamical preference for complete decomposition to separated fragments at higher energies.

In the present case, the long-range region can be separated into two intermediates: a $CH_3\cdots NO_2$ intermediate, I_N, where the methyl group is closer to the N than either of the O's, and a $CH_3\cdots ONO$ intermediate, I_O, where the methyl group is instead closer to one or the other of the O atoms. The overall kinetics then reduces to the following system of reactions:

$CH_3NO_2 = CH_3\ldots NO_2$	$N_{inner,N}$
$CH_3\ldots NO_2 = CH_3 + NO_2$	$N_{outer,N}$
$CH_3\ldots NO_2 = CH_3\ldots ONO$	$N_{roaming}$
$CH_3\ldots ONO = CH_3 + NO_2$	$N_{outer,O}$
$CH_3\ldots ONO = CH_3ONO$	$N_{inner,O}$

where the N terms represent the reactive flux for the specified channel. This case is closely related to that for CH_3CHO, but with isomerization products replacing the abstraction products. The inner and outer fluxes for the two sides are readily estimated with our variable reaction coordinates TST method-

DOI: 10.1021/acs.jpca.5b01563
J. Phys. Chem. A 2015, 119, 7872−7893

ologies. Meanwhile, the roaming flux can be estimated as the flux through the vertical planar surface with $x \sim 0.5$ Å (cf. Figures 15 and 16).

Even for this simplest of cases, the branching between roaming mediated isomerization ($CH_3NO_2 \rightarrow CH_3ONO$), k_{RMI}, and dissociation ($CH_3NO_2 \rightarrow CH_3 + NO_2$), k_{diss}, is given by a fairly complex expression:

$$k_{RMI}/k_{diss} = N_{inner,O}/[N_{outer,O}(1 + N_{outer,N}/N_{roaming}) + N_{outer,N}(1 + N_{inner,O}/N_{roaming})]$$

Nevertheless, this expression is readily evaluated. The individual fluxes for RMI and dissociation are given by

$$N_{RMI} = N_{inner,N}N_{inner,O}N_{roaming} /[(N_{outer,N} + N_{inner,N} + N_{roaming}) \times (N_{outer,O} + N_{inner,O} + N_{roaming}) - N_{roaming}{}^2]$$

$$N_{diss} = N_{inner,N}[N_{outer,N}(N_{outer,O} + N_{inner,O} + N_{roaming}) + N_{outer,O}N_{roaming}]/[(N_{outer,N} + N_{inner,N} + N_{roaming}) \times (N_{outer,O} + N_{inner,O} + N_{roaming}) - N_{roaming}{}^2]$$

respectively.

Notably, at energies below the dissociation threshold the expression for k_{RMI}/k_{diss} correctly yields an infinite branching because $N_{outer,N}$ and $N_{outer,O}$ are necessarily 0. Furthermore, with increasing energy above the dissociation threshold both $N_{outer,N}$ and $N_{outer,O}$ rapidly become competitive with (or even dominates) both $N_{inner,O}$ and $N_{roaming}$ and the roaming branching fraction rapidly decays to a small number. This result clearly demonstrates the threshold nature of the roaming phenomenon. Roaming is a dominant process only from its threshold to just above the dissociation threshold.

It is instructive to review various limits for these expressions. The rapid roaming (RR) limit corresponds to the case where $N_{roaming}$ is much greater than both $N_{outer,N}$ and $N_{inner,O}$. In this limit, the RMI branching becomes proportional to the flux going in to CH_3ONO from $CH_3\cdots ONO$ relative to the total flux going from I_N and I_O out to $CH_3 + NO_2$.

$$k_{RMI}/k_{diss} \rightarrow N_{inner,O}/(N_{outer,N} + N_{outer,O})$$

The individual fluxes are given by

$$N_{RMI} = N_{inner,N}N_{inner,O} /(N_{outer,N} + N_{inner,N} + N_{outer,O} + N_{inner,O})$$

$$N_{diss} = N_{inner,N}(N_{outer,N} + N_{outer,O}) /(N_{outer,N} + N_{inner,N} + N_{outer,O} + N_{inner,O})$$

Within the statistical framework, this limit is generally applicable only at energies near the dissociation threshold. But this energy range is precisely the interesting range of energies where the branching switches from dominantly roaming to dominantly dissociation. At higher energies $N_{outer,N}$ generally becomes competitive with $N_{roaming}$ because they have a similar entropy. At lower energies $N_{inner,O}$ competes with $N_{roaming}$ because the inner transition lies at separations where the minimum on the inner TS dividing surface is typically comparable to or lower than the minimum on the roaming dividing surface.

In the slow roaming (SR) limit, where $N_{roaming}$ is much less than both $N_{outer,N}$ and $N_{outer,O}$, the branching is proportional to the roaming flux, $N_{roaming}$:

$$k_{RMI}/k_{diss} \rightarrow N_{roaming}N_{inner,O}/[N_{outer,N}(N_{outer,O} + N_{inner,O})]$$

The individual fluxes are given by

$$N_{RMI} = N_{inner,N}N_{roaming}N_{inner,O}/[(N_{outer,N} + N_{inner,N}) (N_{outer,O} + N_{inner,O})]$$

$$N_{diss} = N_{inner,N}N_{outer,N}/(N_{outer,N} + N_{inner,N})$$

In this limit, the roaming flux is proportional to the probability of roaming $[N_{roaming}/(N_{outer,N} + N_{inner,N})]$ times the probability of addition to the O $[N_{inner,O}/(N_{outer,O} + N_{inner,O})]$. Interestingly, at low energies this roaming flux reduces to just $N_{roaming}$ because the inner fluxes dominate the outer fluxes at low energy. Meanwhile, in this same limit, the dissociative flux reduces to $N_{outer,N}$ and the branching reduces to $N_{roaming}/N_{outer,N}$. Nevertheless, at least within the statistical framework the slow roaming conditions are rarely met, except perhaps at high energy for some reactions.

In a rapid O addition (ROA) limit, we instead consider $N_{inner,O}$ to be large, and the branching expression reduces to

$$k_{RMI}/k_{diss} \rightarrow N_{roaming}/N_{outer,N}$$

The individual fluxes are given by

$$N_{RMI} = N_{inner,N}N_{roaming}/(N_{outer,N} + N_{inner,N} + N_{roaming})$$

$$N_{diss} = N_{inner,N}N_{outer,N}/(N_{outer,N} + N_{inner,N} + N_{roaming})$$

This limit is increasingly valid with decreasing energy, particularly below the dissociation threshold because the effective TS energy for the inner transition states generally lies below the roaming threshold. Interestingly, this limit for k_{RMI}/k_{diss} is the same as the low energy limit of the slow roaming limit.

In their analysis Zhu et al.[15] ignore any coupling of the channels and evaluate the fluxes as

$$N_{RMI} = N_{roaming}$$

$$N_{diss} = \min(N_{inner,N}, N_{outer,N})$$

This decoupling limit ignores the bottleneck to formation of the long-range intermediate that must precede roaming and the inner bottleneck to addition to the O. It thereby provides an upper limit for the RMI flux. Notably, this result for k_{RMI}/k_{diss} is the same as the low energy limits for the slow roaming and rapid O addition expressions.

The various statistical and trajectory fluxes are illustrated in Figures 17−19. The outer and inner statistical theory fluxes for the N side are seen to provide an accurate representation of the trajectory flux for the decomposition of CH_3NO_2 into $CH_3 + NO_2$ at low and high energies, respectively. The transition from a dominant outer to a dominant inner transition state is seen to occur at about 1.5 kcal/mol. A similar correspondence is found for the O side, but with a more gradual transition between the inner and outer transition states.

The plot in Figure 19 compares the various expressions for the statistical RMI flux, N_{RMI}, with both the full statistical model

DOI: 10.1021/acs.jpca.5b01563
J. Phys. Chem. A 2015, 119, 7872−7893

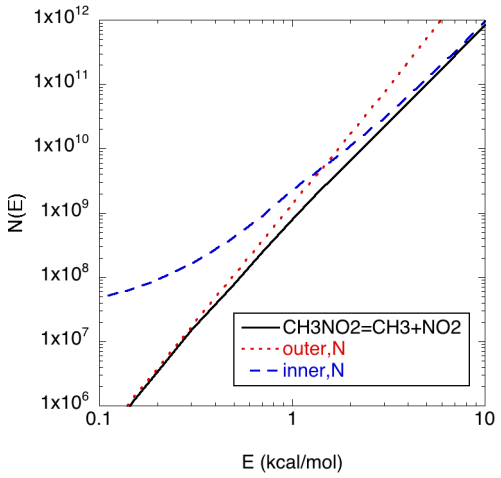

Figure 17. Plot of the statistical and trajectory fluxes for CN fission in CH_3NO_2.

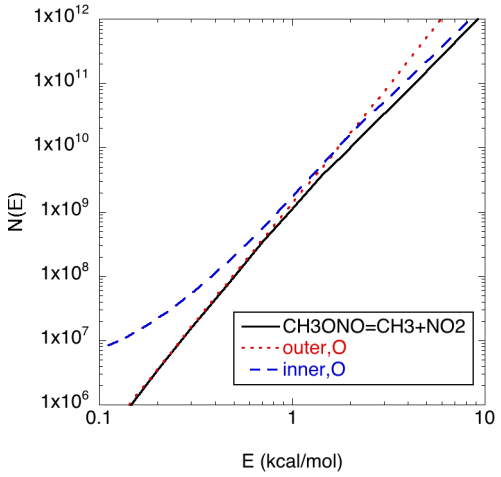

Figure 18. Plot of the statistical and trajectory fluxes for CO fission in CH_3ONO.

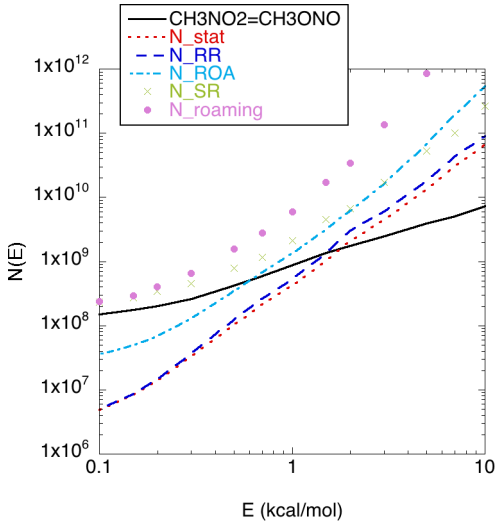

Figure 19. Plot of various statistical approximations and the RBT flux for the RMI in CH_3NO_2.

and RBT results (solid line). Notably, the rapid roaming limit (N_RR) provides a fairly accurate reproduction of the full statistical flux (N_stat) over the full energy range plotted. Meanwhile, the roaming flux alone (N_roaming), which is employed as the RMI flux in the decoupled limit of Zhu et al., is at least an order of magnitude greater than the statistical predictions. The rapid O addition limit (N_ROA) is also never a valid approximation to the full statistical model, at least for the energy range plotted. With increasing energy the slow roaming limit (N_SR) gradually transitions from the roaming only flux, toward the full statistical flux.

The comparison of the full statistical model with the RBT flux suggests that there is a dynamical preference for RMI at low energies, and against it at high energies. The latter is readily explained in terms of a dynamical preference toward continued dissociation at high reaction coordinate energies. In contrast, the former suggests a dynamical preference at low translational energies for full exploration of orientational roaming followed by O addition prior to the statistical sampling of the dissociation paths. Interestingly, at low energies the RBT flux approaches the roaming only flux, suggesting that the roaming bottleneck really is the correct bottleneck for the RMI process at low energy.

The present RBT and statistical model predictions for the RMI branching $[P_{RMI} = N_{RMI}/(N_{RMI} + N_{diss})]$ are compared in Figure 20 with the corresponding predictions from the

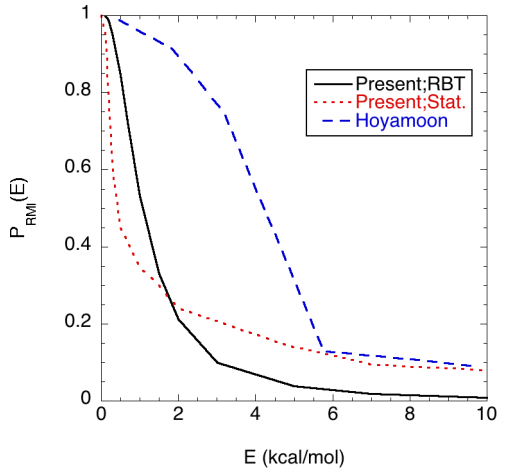

Figure 20. Plot of the predicted RMI probability as a function of the energy relative to $CH_3 + NO_2$. The solid black line denotes the present RBT results, the red dotted line denotes the present statistical theory results, and the dashed blue line denotes the full dimensional quasiclassical trajectory results of Hoyamoon et al.[35]

quasiclassical trajectory simulations of Hoyamoon et al.[35] The latter is obtained as the sum of the branching to the CH_3O + NO and CH_2O + HNO channels, both of which must be preceded by the RMI process because the tight isomerization TS is too high in energy to allow significant flux. Although the three results show qualitatively similar behaviors, quantitatively they are very different. The deviation between the statistical and RBT results is as discussed above with regard to Figure 19.

It is important to recognize that the roaming phenomenon is a threshold phenomenon. By focusing on only the transitional modes, the present RBT approach should provide an accurate treatment of this threshold behavior. The modes being considered are relative and overall rotational modes, whose thresholds are properly treated in a classical framework. The quantum thresholds of the vibrational modes of the fragments

DOI: 10.1021/acs.jpca.5b01563
J. Phys. Chem. A 2015, 119, 7872−7893

enter naturally through convolutions of the properly determined transitional mode fluxes.

In contrast, full-dimensional quasiclassical trajectory simulations must make some assumption about how conservation of the conserved mode vibrational zero-point energy affects the dynamics. This assumption strongly affects the predicted roaming. Indeed, for the PES employed in ref 35 a quasiclassical study with strict conservation of zero-point energy at all times would have predicted zero-roaming at the dissociation threshold, because the zero-point-corrected roaming threshold on their PES is actually 0.23 kcal/mol higher than the dissociation threshold. In this situation, the dissociative flux should always dominate the roaming flux and one would expect only a small peak in the predicted roaming just above the roaming threshold, followed by a decay back toward 0. Meanwhile, a purely classical simulation would likely predict a RMI branching that rapidly decays from unity toward zero as the energy increases just a few tenths of a kcal/mol above the dissociation threshold, because the roaming threshold on their PES is very close to the dissociation threshold.

In their simulations, Hoyamoon et al.[35] instead adopt what they call a "soft-constraint" where all trajectories are discarded if the products are formed with less than their harmonic zero-point energy. This constraint artificially biases against dissociation because it only affects dissociative trajectories; isomerizing trajectories are so exothermic that effectively all of them satisfy the zero-point constraint by the time products are reached. This biasing leads to too gradual a rise in the dissociative flux relative to the roaming mediated isomerization flux and the roaming branching is greatly overestimated, as is observed in Figure 20.

Zhu et al.[37] also predict this branching fraction. The scale of their plot makes it difficult to be precise, but it appears that their predicted roaming branching falls more rapidly even than the present statistical predictions. Furthermore, it falls to effectively 0 within 2 kcal/mol of the threshold. The latter behavior seems counter to expectations. It appears that their roaming transition state has an entropy similar to that of their dissociation transition state, and thus their branching should gradually decrease at high energies just as with the current statistical model results.

5.3. Thermal Kinetics. The pressure dependent RMI branching fractions from the present RBT/ME approach and from Zhu et al.[15] are illustrated in Figure 21 for Ar bath gas. The roaming branching is predicted to be significant for a broad range of temperature and pressure. At 1 atm pressure it is still 17% at 500 K and 9% at 2000 K. Qualitatively, the two predictions show many similarities, with both decreasing with increasing temperature and with increasing pressure. The decrease with temperature arises because the microcanonical roaming probability decreases dramatically with increasing energy (cf. Figure 20). More energetic trajectories are more likely to proceed directly on to products. The decrease with pressure arises because the average energy at which the dissociation occurs increases with increasing pressure. In the low pressure limit, the dissociative distribution is a narrow band starting at the roaming threshold with a width determined by the decay of the energy transfer kernel, i.e., just a few kcal/mol. This narrow distribution of energy is precisely that set of energies for which roaming is dominant.

The results of Zhu et al.[15] are generally smaller than the present results and they also show a much stronger pressure dependence. In their analysis, Zhu et al., consider the roaming

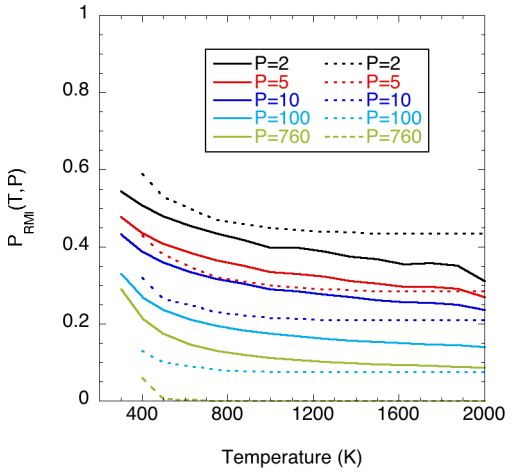

Figure 21. Plot of the predicted temperature and pressure dependence of the RMI probability in an Ar bath gas at the specified pressures (Torr) from the present RBT/ME approach (solid lines) and from Zhu et al.[15] (dotted lines).

and dissociation processes to be completely separate. Within the statistical framework, this assumption should yield an overestimate of the branching fraction. However, the statistical framework itself underestimates the RMI branching; for the T and P range of relevance to the present experiments the complete statistical model underestimates the branching relative to the RBT model by about a factor of 0.6. A further shortcoming in their analysis is their use of rigid-rotor harmonic oscillator assumptions to evaluate the roaming fluxes.[15] Such estimates are generally expected to be of relatively limited accuracy for the treatment of roaming processes.[89] Here, within the statistical framework, replacing the phase-space-integration-based evaluation of the roaming flux with a rigid-rotor harmonic-oscillator analysis lowers the predicted RMI branching by a factor of 2−3.

Nevertheless, it is still puzzling that the Zhu et al. branching ratio is so low, especially when one realizes that they have used their low energy CASPT3 roaming saddle point of −2.7 kcal/mol (relative to CH_3 + NO_2) in their calculations. Our predicted RMI branching is quite sensitive to this energy. For example, shifting the roaming flux versus energy down by 0.2 kcal/mol, which is representative of the uncertainty in the PES, yields RMI branching fractions that are increased by about a factor of 1.2.

As discussed in the PES results, our best estimate for the zero-point-corrected roaming saddle point energy is −0.78 kcal/mol. In contrast, the analytic potential energy surface has a ZPE-corrected saddle point energy of −0.98 kcal/mol. To first order, this discrepancy has the effect of shifting the calculated roaming flux versus energy curve by 0.20 kcal/mol. At low energies the RBT calculated RMI flux is fairly similar to the roaming flux. Thus, a crude correction for the effect of this discrepancy on the kinetics is to simply shift the calculated RMI flux by 0.20 kcal/mol. All the thermal kinetics calculations reported here employ this shift.

It is difficult to accurately predict the uncertainty in our theoretical estimates. Nevertheless, we feel it is useful to provide some qualitative predictions of our expectations. On the basis of the observed variations in the MEP energies and the accuracy of the potential energy surface fits, we expect our prediction of the high pressure limit addition/dissociation rate

DOI: 10.1021/acs.jpca.5b01563
J. Phys. Chem. A 2015, 119, 7872−7893

constants to have a 2σ uncertainty of perhaps 20−30%. Numerous comparisons of comparable VRC-TST calculations with experiment for related reactions suggest that such uncertainty estimates are reasonable. The evaluation of the pressure dependence of the kinetics relies to some extent on the accuracy of our treatment of energy transfer, which involves a fit to the experimental data. This accuracy thus depends to some extent on the accuracy of the underlying experiment. Similarly, the prediction of the RMI rate constant is more involved, requiring a treatment of the roaming dynamics in addition to the pressure dependence. Thus, the 2σ uncertainties for both the pressure dependent rate constants and the roaming branching are perhaps twice as large, i.e., a factor of 1.6.

As illustrated in Figure 7, the present RBT/ME-based predictions for the temperature and pressure dependence of the rate coefficient for dissociation of CH_3NO_2 into CH_3 + NO_2, can provide an excellent representation of the present laser schlieren data. These data are for Kr as a bath gas and employed an optimized α_{300} value of 320 cm^{-1}. A similar attempt to fit the data of Zaslonko[23] for Ar bath gas at somewhat lower temperatures (1050−1400 K) (cf. Figure 22),

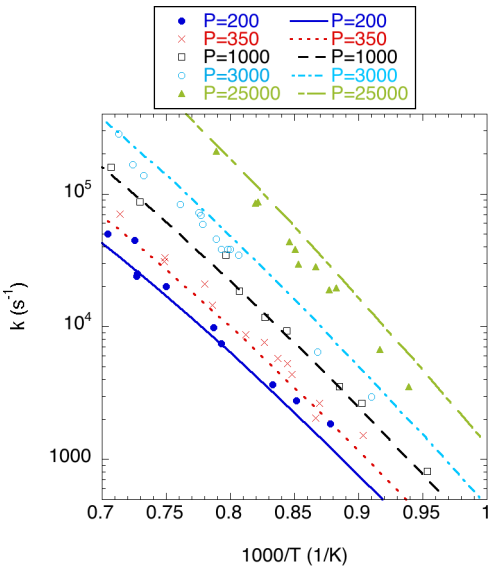

Figure 22. Arrhenius plot of the total rate coefficient for CH_3NO_2 decomposition (k_1 + k_2) at a variety of pressures from the present RBT/ME calculations (lines) and from Zaslonko et al.[23] (symbols).

yielded an optimal α_{300} value of 200 cm^{-1}. For this value, the observations from various other studies in Ar bath gas, such as that of Glanzer et al.[27] and of Petrov et al.,[21] are also well reproduced (cf. Figure 23). A number of low temperature observations have also been made with CH_3NO_2 as the bath gas.[28−33] In this case, the predictions are near the high pressure limit (cf. Figure 23), which is not unreasonable given the enhanced energy transfer rates for a collider such as CH_3NO_2.

Although it is not unreasonable for Ar and Kr to have slightly different energy transfer parameters, prior trajectory simulations for a variety of systems have shown similar energy transfer properties for Ar and Kr, with α_{300} differing typically by less than 5%.[87,90] Thus, it seems likely that the somewhat larger discrepancy in these fitted α_{300} values is simply indicative of the level of accuracy of the experimental data. Certainly, both of these values are within the range of what one might expect on the basis of our prior studies of related molecules, particularly

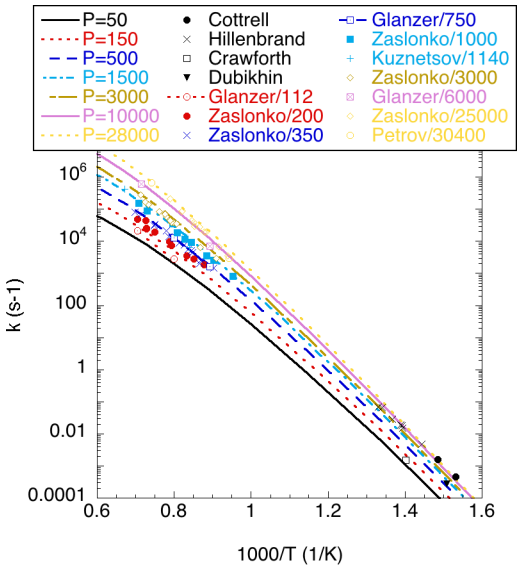

Figure 23. Arrhenius plot of the total rate coefficient for CH_3NO_2 decomposition (k_1 + k_2) at a variety of temperatures and pressures from the present RBT/ME calculations (lines) and from a variety of experiments.

when one notes that this parameter generally increases with molecular size.

As discussed at length in the experimental section, the RBT/ME predictions for the branching ratio are also in reasonable accord with the present laser schlieren measurements, especially when one accounts for reasonable variations in the CH_3 + NO_2 reaction, and for the uncertainties in the theoretical predictions.

The RBT/ME simulations also yield predictions for the rate of the recombination reactions CH_3 + NO_2 → CH_3NO_2 and CH_3 + NO_2 → CH_3ONO, with the latter correlating with measurements of k_{61}. For the former reaction, we predict a room temperature high pressure limit rate coefficient of 3.8 × 10^{-11} cm^3 $molecule^{-1}$ s^{-1}, which is in excellent agreement with the corresponding experimental data for this reaction (3.26 ± 0.40,[91] 3.45 ± 0.50,[90] 2.0 ± 1.0,[92] 4.3 ± 0.4[93]) × 10^{-11} cm^3 $molecule^{-1}$ s^{-1}. Meanwhile, for the 1100−1400 K range, Glanzer and Troe extract a value of 3.43 × 10^{-11} cm^3 $molecule^{-1}$ s^{-1},[94] whereas the RBT/ME simulations predict a value of 1.9 × 10^{-11}. For CH_3 + NO_2 → CH_3ONO the RBT/ME predictions for the high pressure rate coefficient are compared with the available experimental data for k_{61}[22,54,95,96] in Figure 10. In this case, it appears that the RBT/ME predictions are about a factor of 2 too large near room temperature and remain somewhat high at higher temperature, although at higher temperature the experimental record is less clear. The extent of this discrepancy is somewhat surprising. It is perhaps worth noting that, according to the statistical theory framework, an overestimate of k_{61} would generally map into a related overestimate of the RMI.

For modeling purposes we provide in Table 5 modified Arrhenius fits to the present RBT/ME calculations of the rate constants for CH_3NO_2 → CH_3 + NO_2 and CH_3NO_2 → roaming products at a range of pressures with our best fit for Kr bath gas. Though we recognize that it would be valuable to also predict the pressure dependence of the branching between CH_3ONO and bimolecular products, this aspect requires an accurate treatment of the CH_3ONO → CH_3O + NO and

DOI: 10.1021/acs.jpca.5b01563
J. Phys. Chem. A 2015, 119, 7872−7893

Table 5. Modified Arrhenius Fits for the Rate Constants for $CH_3NO_2 \rightarrow CH_3 + NO_2$ and $CH_3NO_2 \rightarrow$ Roaming Products[a]

reaction	pressure (atm)	A (s^{-1})	n	E_a (cal/mol)	T range (K)
$CH_3NO_2 \rightarrow CH_3 + NO_2$	0.001	6.59×10^{50}	−11.99	68620	500−2000
	0.003	4.18×10^{51}	−12.07	68970	500−2000
	0.01	2.58×10^{52}	−12.13	69450	500−2000
	0.03	1.00×10^{53}	−12.14	69950	500−2000
	0.1	3.02×10^{53}	−12.11	70570	500−2000
	0.3	5.11×10^{53}	−12.03	71160	500−2000
	1	4.15×10^{53}	−11.84	71780	500−2000
	3	1.20×10^{53}	−11.53	72230	500−2000
	10	6.07×10^{51}	−10.99	72450	500−2000
	30	5.96×10^{49}	−10.27	72260	500−2000
	100	3.70×10^{46}	−9.20	71520	500−2000
$CH_3NO_2 \rightarrow$ roaming products	0.001	9.05×10^{52}	−12.73	68940	500−2000
	0.003	1.34×10^{53}	−12.66	69120	500−2000
	0.01	1.95×10^{53}	−12.57	69400	500−2000
	0.03	2.69×10^{53}	−12.50	67200	500−2000
	0.1	2.97×10^{53}	−12.39	70130	500−2000
	0.3	2.11×10^{53}	−12.23	70500	500−2000
	1	6.73×10^{52}	−11.96	70820	500−2000
	3	8.64×10^{51}	−11.60	70970	500−2000
	10	2.37×10^{50}	−11.03	70870	500−2000
	30	3.52×10^{48}	−10.39	70680	500−2000
	100	1.91×10^{46}	−9.62	70620	500−2000

[a]Rate coefficient is given by $AT^n \exp(-E_a/RT)$ where T is in K.

H_2CO + HNO fluxes. Such a treatment was deemed beyond the scope of the present analysis.

6. CONCLUSIONS

Loss of nitromethane through unimolecular reactions at high temperatures is a far from trivial process that is complicated by competition between dissociation to CH_3 + NO_2 products and a roaming mediated isomerization that predominantly leads, eventually, to H_2CO + NO + H. Analysis of the LS density gradients is complicated by the dissociation and RMI paths having similar effective enthalpies of reaction which reduces the sensitivity to the branching fraction. Typically, dissociation and roaming paths have very large differences in their ΔH_r as one forms radical products and the other stable molecules.

The associated reaction of CH_3 + NO_2 is also not trivial to analyze and leads not to nitromethane but rather CH_3O + NO or CH_2O + HNO. The current experimental results are consistent with the evaluation of Glarborg et al., whereas the theoretical predictions are about a factor of 2.5 higher. However, both are consistent with the extant sparse high temperature literature for this reaction. Further theoretical and experimental study of this process is warranted but beyond the scope of this work.

The current theoretical study has developed a high level framework for this challenging system based around a global PES for CH_3···NO_2. A careful analysis with particular attention to the features that most influence the roaming channel has resulted in kinetic and mechanistic parameters that are in reasonable to very good agreement with the current experimental work. In particular, the experimental rates of dissociation of nitromethane are readily reproduced by the theoretical predictions and the predicted branching to RMI is entirely consistent with models for the time dependence of the density gradients. There is, however, some modest disagreement on the magnitude of the energy transfer parameter needed to reproduce the current work in krypton bath gas and the experimental literature for argon as a bath gas. At this time this cannot be resolved, but the differences lie well within the uncertainties of the theoretical work and may be entirely due to uncertainties in the different experiments.

The present theoretical analysis improves on prior theoretical analyses of the roaming process of Homayoon et al.[35] and of Zhu et al.[15] in the incorporation of more quantitatively accurate potential energy surface information and in the focus on the full roaming, dissociation, and isomerization dynamics within the reduced dimensional rigid body space. The resulting high level predictions for the branching to RMI are dramatically different from those of Homayoon et al.[35] Meanwhile, the predictions of Zhu et al. for the RMI branching at high temperatures and low pressures (P < 200 Torr) are qualitatively consistent with the current work. However, Zhu et al. do predict much stronger pressure dependence in the branching ratio than observed experimentally or predicted theoretically. The theoretical effort also reviews a statistical model for the overall decomposition process that is helpful in interpreting the details of the kinetic behavior.

Overall, the current work provides a consistent picture of the dissociation of nitromethane and the magnitude of the RMI channel as well as the temperature and pressure dependence of this path based on detailed complementary experimental and theoretical work.

■ ASSOCIATED CONTENT

Supporting Information

The following items are available in the electronic Supporting Information: (1) shock conditions and experimental rate coefficients; (2) complete reaction mechanism; (3) ATcT heats of formation for key species; (4) NASA polynomials for key species. This material is available free of charge via the Internet at http://pubs.acs.org

DOI: 10.1021/acs.jpca.5b01563
J. Phys. Chem. A 2015, 119, 7872−7893

AUTHOR INFORMATION

Corresponding Authors

*S. J. Klippenstein. E-mail: sjk@anl.gov.
*R. S. Tranter. E-mail: Tranter@anl.gov.

Present Address

§Space Vehicles Directorate, Air Force Research Laboratory, Kirtland AFB, New Mexico 87117.

Author Contributions

The manuscript was written through contributions of all authors. All authors have given approval to the final version of the manuscript. C.J.A. and J.B.R. contributed equally.

Notes

The authors declare no competing financial interest.

ACKNOWLEDGMENTS

This material is based upon work supported by the U.S. Department of Energy, Office of Science, Office of Basic Energy Sciences, Division of Chemical Sciences, Geosciences, and Biosciences. The work at Argonne was supported under Contract No. DE-AC02-06CH11357. Sandia is a multiprogram laboratory operated by Sandia Corporation, a Lockheed Martin Company, for the United States Department of Energy under Contract No. DE-AC04-94-AL85000. Support for S.J.K. was provided by the Army Research Office under Grant W911NF1310251 as part of their Molecular Structure and Dynamics program.

REFERENCES

(1) Townsend, D.; Lahankar, S. A.; Lee, S. K.; Chambreau, S. D.; Suits, A. G.; Zhang, X.; Rheinecker, J.; Harding, L. B.; Bowman, J. M. The Roaming Atom: Straying from the Reaction Path in Formaldehyde Decomposition. *Science* **2004**, *306*, 1158−1161.

(2) Suits, A. G. Roaming Atoms and Radicals: A New Mechanism in Molecular Dissociation. *Acc. Chem. Res.* **2008**, *41*, 873−881.

(3) Harding, L. B.; Georgievskii, Y.; Klippenstein, S. J. Roaming Radical Kinetics in the Decomposition of Acetaldehyde. *J. Phys. Chem. A* **2010**, *114*, 765−777.

(4) Harding, L. B.; Klippenstein, S. J. Roaming Radical Pathways for the Decomposition of Alkanes. *J. Phys. Chem. Lett.* **2010**, *1*, 3016−3020.

(5) Klippenstein, S. J.; Georgievskii, Y.; Harding, L. B. Statistical Theory for the Kinetics and Dynamics of Roaming Reactions. *J. Phys. Chem. A* **2011**, *115*, 14370−14381.

(6) Herath, N.; Suits, A. G. Roaming Radical Reactions. *J. Phys. Chem. Lett.* **2011**, *2*, 642−647.

(7) Bowman, J. M. Roaming. *Mol. Phys.* **2014**, *112*, 2516−2526.

(8) Sivaramakrishnan, R.; Michael, J. V.; Klippenstein, S. J. Direct Observation of Roaming Radicals in the Thermal Decomposition of Acetaldehyde. *J. Phys. Chem. A* **2010**, *114*, 755−764.

(9) Sivaramakrishnan, R.; Su, M. C.; Michael, J. V.; Klippenstein, S. J.; Harding, L. B.; Ruscic, B. Shock Tube and Theoretical Studies on the Thermal Decomposition of Propane: Evidence for a Roaming Radical Channel. *J. Phys. Chem. A* **2011**, *115*, 3366−3379.

(10) Sivaramakrishnan, R.; Michael, J. V.; Wagner, A. F.; Dawes, R.; Jasper, A. W.; Harding, L. B.; Georgievskii, Y.; Klippenstein, S. J. Roaming Radicals in the Thermal Decomposition of Dimethyl Ether: Experiment and Theory. *Combust. Flame* **2011**, *158*, 618−632.

(11) Sivaramakrishnan, R.; Michael, J. V.; Harding, L. B.; Klippenstein, S. J. Shock Tube Explorations of Roaming Radical Mechanisms: The Decompositions of Isobutane and Neopentane. *J. Phys. Chem. A* **2012**, *116*, 5981−5989.

(12) Tranter, R. S.; Lynch, P. T.; Yang, X. Dissociation of Dimethyl Ether at High Temperatures. *Proc. Combust. Inst.* **2013**, *34*, 591−598.

(13) Rosado-Reyes, C. M.; Tsang, W. Thermal Stability of Larger Carbonyl Compounds: 2-Methylbutyraldehyde. *Int. J. Chem. Kinet.* **2014**, *46*, 285−293.

(14) Prozument, K.; Suleimanov, Y. V.; Buesser, B.; Oldham, J. M.; Green, W. H.; Suits, A. G.; Field, R. W. A Signature of Roaming Dynamics in the Thermal Decomposition of Ethyl Nitrite: Chirped-Pulse Rotational Spectroscopy and Kinetic Modeling. *J. Phys. Chem. Lett.* **2014**, *5*, 3641−3648.

(15) Zhu, R. S.; Raghunath, P.; Lin, M. C. Effect of Roaming Transition States upon Product Branching in the Thermal Decomposition of CH_3NO_2. *J. Phys. Chem. A* **2013**, *117*, 7308−7313.

(16) Dey, A.; Fernando, R.; Abeysekera, C.; Homayoon, Z.; Bowman, J. M.; Suits, A. G. Photodissociation Dynamics of Nitromethane and Methyl Nitrite by Infrared Multiphoton Dissociation Imaging with Quasiclassical Trajectory Calculations: Signatures of the Roaming Pathway. *J. Chem. Phys.* **2014**, *140*, 054305.

(17) Kuznetsov, N.; Petrov, Y.; Turetskii, S. V. Analysis of Nitromethane Thermal Decomposition at Low Temperatures. *Kinet. Catal.* **2013**, *54*, 131−138.

(18) Rodriguez, J. D.; Gonzalez, M. G.; Rubio-Lago, L.; Batares, L.; Samartzis, P. C.; Kitsopoulos, T. N. Stereodynamics of the Photodissociation of Nitromethane at 193 nm: Unravelling the Dissociation Mechanism. *J. Phys. Chem. A* **2013**, *117*, 8175−8183.

(19) Kohge, Y.; Hanada, T.; Sumida, M.; Yamasaki, K.; Kohguchi, H. Photodissociation Dynamics of Nitromethane at 213 nm Studied by Ion-Imaging. *Chem. Phys. Lett.* **2013**, *556*, 49−54.

(20) Kuznetsov, N.; Petrov, Y.; Turetskii, S. V. Kinetics of NO_2 Formation upon the Decomposition of Nitromethane behind Shock Waves and the Possibility of Nitromethane Isomerization in the Course of the Reaction. *Kinet. Catal.* **2012**, *53*, 1−12.

(21) Petrov, Y.; Karasevich, Y.; Turetskii, S. V. Decomposition of Nitromethane in Shock Waves; The Primary State and the Kinetics of Decomposition at Pressures of about 40 atm. *Russ. J. Phys. Chem. B* **2010**, *4*, 566−573.

(22) Glarborg, P.; Bendtsen, A. B.; Miller, J. A. Nitromethane Dissociation: Implications for the CH_3 + NO_2 Reaction. *Int. J. Chem. Kinet.* **1999**, *31*, 591−602.

(23) Zaslonko, I. S.; Petrov, Y. P.; Smirnov, V. N. Thermal Decomposition of Nitromethane in Shock Waves: The Effect of Pressure and Collision Partners. *Kinet. Catal.* **1997**, *38*, 321−324.

(24) Zhang, Y. X.; Bauer, S. H. Modeling the Decomposition of Nitromethane, Induced by Shock Heating. *J. Phys. Chem. B* **1997**, *101*, 8717−8726.

(25) Wodtke, A. M.; Hintsa, E. J.; Lee, Y. T. Infrared Multiphoton Dissociation of 3 Nitroalkanes. *J. Phys. Chem.* **1986**, *90*, 3549−3558.

(26) Hsu, D. S. Y.; Lin, M. C. Laser Probing and Kinetic Modeling of NO and CO Production in Shock-Wave Decomposition of Nitromethane under Highly Diluted Conditions. *J. Energy Mater.* **1985**, *3*, 95−127.

(27) Glanzer, K.; Troe, J.; Thermische Zerfallsreaktionen von Nitroverbindungen, I. Dissoziation von Nitromethan. *Helv. Chim. Acta* **1972**, *55*, 2884−2893.

(28) Dubikhin, V. V.; Nazin, G. M.; Manelis, G. B. Thermal Decomposition of Nitromethane. *Inst. Chem. Phys. Acad. Sci. USSR* **1971**, *6*, 1247−1249.

(29) Crawforth, C. G.; Waddington, D. J. Reactions of Nitroalkanes in the Gas Phase. Part 1. Pyrolysis of Nitromethane. *Trans. Faraday Soc.* **1969**, *65*, 1334−1349.

(30) Hillenbrand, L. J.; Kilpatrick, M. L. The Thermal Decomposition of Nitromethane. *J. Chem. Phys.* **1953**, *21*, 525−535.

(31) Hillenbrand, L. J.; Kilpatrick, M. L. The Thermal Decomposition of Nitromethane. *J. Chem. Phys.* **1951**, *19*, 381.

(32) Cottrell, T. L.; Graham, T. E.; Reid, T. J. The Thermal Decomposition of Nitromethane. *Trans. Faraday Soc.* **1951**, *47*, 584−590.

(33) Cottrell, T.; Reid, T. The Thermal Decomposition of Nitromethane. *J. Chem. Phys.* **1950**, *18*, 1306.

(34) Isegawa, M.; Lie, F.; Maeda, S.; Morokuma, K. Ab Initio Reactions Pathways for the Photodissociation and Isomerization of

DOI: 10.1021/acs.jpca.5b01563
J. Phys. Chem. A 2015, 119, 7872−7893

Nitromethane on Four Singlet Potential Energy Surfaces with Three Roaming Paths. *J. Chem. Phys.* **2014**, *140*, 244310.
(35) Homayoon, Z.; Bowman, J. M. Quasiclassical Trajectory Study of CH_3NO_2 Decomposition via Roaming Mediated Isomerization Using a Global Potential Energy Surface. *J. Phys. Chem. A* **2013**, *117*, 11665−11672.
(36) Homayoon, Z.; Bowman, J. M.; Dey, A.; Abeysekera, C.; Fernando, R.; Suits, A. G. Experimental and Theoretical Studies of Roaming Dynamics in the Unimolecular Dissocation of CH_3NO_2 to CH_3O + NO. *Z. Phys. Chem.* **2013**, *227*, 1267−1280.
(37) Zhu, R. S.; Lin, M. C. CH_3NO_2 Decomposition/Isomerization Mechanism and Product Branching Ratios: An *Ab Initio* Chemical Kinetic Study. *Chem. Phys. Lett.* **2009**, *478*, 11−16.
(38) Nguyen, M. T.; Le, H. T.; Hajgato, B.; Veszpremi, T.; Lin, M. C. Nitromethane-Methyl Nitrite Rearrangement: A Persistent Discrepancy between Theory and Experiment. *J. Phys. Chem. A* **2003**, *107*, 4286−4291.
(39) Hu, W. F.; He, T. J.; Chen, D. M.; Liu, F. C. Theoretical Study of the CH_3NO_2 Unimolecular Decomposition Potential Energy Surface. *J. Phys. Chem. A* **2002**, *106*, 7294−7303.
(40) Saxon, R. P.; Yoshimine, M. Theoretical Study of Nitro Nitrite Rearrangement of CH_3NO_2. *Can. J. Chem.* **1992**, *70*, 572−579.
(41) McKee, M. L. MCSCF Study of the Rearrangement of Nitromethane to Methyl Nitrite. *J. Phys. Chem.* **1989**, *93*, 7365−7369.
(42) McKee, M. L. Ab Initio Study of Rearrangements on the CH_3NO_2 Potential Energy Surface. *J. Am. Chem. Soc.* **1986**, *108*, 5784−5792.
(43) Saxon, R. P.; Yoshimine, M. Theoretical Study of Nitro-Nitrite Rearrangement of NH_2NO_2. *J. Phys. Chem.* **1989**, *93*, 3130−3135.
(44) Kiefer, J. H. In *The Laser Schlieren Technique in Shock Tube Kinetics*; Lifshitz, A., Ed.; Marcel Dekker: New York, 1981; pp 219−277.
(45) Tranter, R. S.; Giri, B. R. A Diaphragmless Shock Tube for High Temperature Kinetic Studies. *Rev. Sci. Instrum.* **2008**, *79*, 094103.
(46) Randazzo, J. B.; Tranter, R. S. An Improved Driver Section for a Diaphragmless Shock Tube. *Rev. Sci. Instrum.* **2015**, *86*, 016117.
(47) Kiefer, J. H.; Manson, A. C. Refractive-Index Change and Curvature in Shock-Waves by Angled Beam Refraction. *Rev. Sci. Instrum.* **1981**, *52*, 1392−1396.
(48) Kiefer, J. H.; Alalami, M. Z.; Hajduk, J. C. Physical Optics of the Laser-Schlieren Shock-Tube Technique. *Appl. Opt.* **1981**, *20*, 221−230.
(49) Gardiner, W. C.; Hidaka, Y.; Tanzawa, T. Refractivity of Combustion Gases. *Combust. Flame* **1981**, *40*, 213−219.
(50) Physical properties obtained from specifications by Sigma Aldrich, released 2015.
(51) Goos, E.; Burcat, A.; Ruscic B. Extended Third Millennium Ideal Gas and Condensed Phase Thermochemical Database for Combustion with updates from Active Thermochemical Tables. http://garfield.chem.elte.hu/Burcat/THERM.DAT. Accessed 6th March 2014.
(52) Dove, J. E.; Troe, J. Theory of Transient Phenomena in Thermal Unimolecular Reactions. *Chem. Phys.* **1978**, *35*, 1−21.
(53) Yang, X.; Goldsmith, C. F.; Tranter, R. S. Decomposition and Vibrational Relaxation in CH_3I and Self-Reaction of CH_3 Radicals. *J. Phys. Chem. A* **2009**, *113*, 8307−8317.
(54) Yang, X.; Jasper, A. W.; Kiefer, J. H.; Tranter, R. S. The Dissociation of Diacetyl: A Shock Tube and Theoretical Study. *J. Phys. Chem. A* **2009**, *113*, 8318−8326.
(55) Srinivasan, N. K.; Su, M. C.; Sutherland, J. W.; Michael, J. V. Reflected Shock Tube Studies of High-Temperature Rate Constants for OH + CH_4 → CH_3 + H_2O and CH_3 + NO_2 → CH_3O + NO. *J. Phys. Chem. A* **2005**, *109*, 1857−1863.
(56) Kendall, R. A.; Dunning, T. H., Jr.; Harrison, R. J. Electron Affinities of the First-Row Atoms Revisited. Systematic Basis Sets and Wavefunctions. *J. Chem. Phys.* **1992**, *96*, 6796−6806.
(57) Celani, P.; Werner, H.-J. Multireference Perturbation Theory for Large Restricted and Selected Active Space Reference Wave Functions. *J. Chem. Phys.* **2000**, *112*, 5546−5557.
(58) Harding, L. B.; Klippenstein, S. J.; Miller, J. A. Kinetics of CH + N_2 Revisited with Multireference Methods. *J. Phys. Chem. A* **2008**, *112*, 522−532.
(59) Moradi, C. P.; Morrison, A. M.; Klippenstein, S. J.; Goldsmith, C. F.; Douberly, G. E. Propargyl + O_2 Reaction in Helium Droplets: Entrance Channel Barrier or Not? *J. Phys. Chem. A* **2013**, *117*, 13626−13635.
(60) Sobol, I. M. *U.S.S.R Comput. Maths. Math. Phys.* **1967**, *16*, 236−242 (in English).
(61) Press, W. H.; Teukolsky, S. A.; Vetterling, W. T.; Flannery, B. P. *Numerical Recipes in Fortran: The Art of Scientific Computing*, 2nd ed.; Cambridge University Press: Cambridge, U.K., 1992.
(62) Braams, B. J.; Bowman, J. M. Permutationally Invariant Potential Energy Surfaces in High Dimensionality. *Int. Rev. Phys. Chem.* **2009**, *28*, 577−606.
(63) Klippenstein, S. J. Variational Optimizations in the Rice-Ramsberger-Kassel-Marcus Theory Calculations for Unimolecular Dissociations with No Reverse Barrier. *J. Chem. Phys.* **1992**, *96*, 367−371.
(64) Georgievskii, Y.; Klippenstein, S. J. Transition State Theory for Multichannel Addition Reactions: Multifaceted Dividing Surfaces. *J. Phys. Chem. A* **2003**, *107*, 9776−9781.
(65) MOLPRO is a Package of Ab Initio Programs written by Werner, H.-J. and Knowles, P. J. with contributions from Almlof, J., Amos, R. D., Berning, A., Cooper, D. L., Deegan, M. J. O., Dobbyn, A. J., Eckert, F., Elbert, S. T., et al.
(66) Werner, H.-J.; Knowles, P. J. A Second Order Multiconfiguration SCF Procedure with Optimal Convergence. *J. Chem. Phys.* **1985**, *82*, 5053−5063.
(67) Knowles, P. J.; Werner, H.-J. An Efficient Second-Order MC-SCF Method for Long Configuration Expansions. *Chem. Phys. Lett.* **1985**, *115*, 259−267.
(68) Hampel, C.; Peterson, K.; Werner, H.-J. A Comparison of the Efficiency and Accuracy of the Quadratic Configuration Interaction (QCISD), Coupled Cluster (CCSD) and Brueckner Coupled Cluster (BCCD) Methods. *Chem. Phys. Lett.* **1992**, *190*, 1−12.
(69) Knowles, P. J.; Hampel, C.; Werner, H.-J. Coupled Cluster Theory for High Spin, Open Shell Reference Wavefunctions. *J. Chem. Phys.* **1993**, *99*, 5219−5227.
(70) Frisch, M. J.; Trucks, G. W.; Schlegel, H. B.; Scuseria, G. E.; Robb, M. A.; Cheeseman, J. R.; Scalmani, G.; Barone, V.; Mennucci, B.; Petersson, G. A.; et al. *Gaussian 09*, Revision A.1; Gaussian, Inc.: Wallingford, CT, 2009.
(71) Stanton, J. F.; Gauss, J.; Harding, M. E.; Szalay P. G.; with contributions from Auer, A. A.; Bartlett, R. J.; Benedikt, U.; Berger, C.; Bernholdt, D. E.; Bomble, Y. J.; et al. and the integral packages *MOLECULE* (Almlöf, J.; Taylor, P. R.), *PROPS* (Taylor, P. R.), *ABACUS* (Helgaker, T.; Jensen, H. J.; Jørgensen, P.; Olsen, J.), and ECP routines by Mitin, A. V.; van Wüllen, C. For the current version, see http://www.cfour.de.
(72) MRCC, a String-Based Quantum Chemical Program Suite; written by M. Kállay. See also: Kállay, M.; Surján, P. R. Higher Excitations in Coupled-Cluster Theory. *J. Chem. Phys.* **2001**, *115*, 2945−2954.
(73) Ruscic, B.; Pinzon, R. E.; Morton, M. L.; von Laszewski, G.; Bittner, S.; Nijsure, S. G.; Amin, K. A.; Minkoff, M.; Wagner, A. F. Introduction to Active Thermochemical Tables: Several "Key" Enthalpies of Formation Revisited. *J. Phys. Chem. A* **2004**, *108*, 9979−9997.
(74) Ruscic, B.; Pinzon, R. E.; von Laszewski, G.; Kodeboyina, D.; Burcat, A.; Leahy, D.; Montoya, D.; Wagner, A. F. Active Thermochemical Tables: Thermochemistry for the 21st Century. *J. Phys. Conf. Ser.* **2005**, *16*, 561−570.
(75) Ruscic, B.; Pinzon, R. E.; Morton, M. L.; Srinivasan, N. K.; Su, M.-C.; Sutherland, J. W.; Michael, J. V. Active Thermochemical Tables: Accurate Enthalpy of Formation of Hydroperoxyl Radical, HO_2. *J. Phys. Chem. A* **2006**, *110*, 6592−6660.

DOI: 10.1021/acs.jpca.5b01563
J. Phys. Chem. A 2015, 119, 7872−7893

(76) Stevens, W. R.; Ruscic, B.; Baer, T. The Heats of Formation of C_6H_5, $C_6H_5^+$, and C_6H_5NO by TPEPICO and Active Thermochemical Tables Analysis. *J. Phys. Chem. A* **2010**, *114*, 13134−13145.
(77) Ruscic, B. Active Thermochemical Tables: Water and Water Dimer. *J. Phys. Chem. A* **2013**, *117*, 11940−11953.
(78) Ruscic, B. Active Thermochemical Tables: Sequential Bond Dissociation Enthalpies of Methane, Ethane, and Methanol and the Related Thermochemistry. *J. Phys. Chem. A* **2015**, DOI: 10.1021/acs.jpca.5b01346.
(79) Ruscic, B.; Feller, D.; Peterson, K. A. Active Thermochemical Tables: Dissociation Energies of Several Homonuclear First-Row Diatomics and Related Thermochemical Values. *Theor. Chem. Acc.* **2014**, *133*, 1415:1−12.
(80) Burcat, A. Thermodynamic Properties of Ideal Gas Nitro and Nitrate Compounds. *J. Phys. Chem. Ref. Data* **1999**, *28*, 63−130.
(81) McBride, B. J.; Gordon, S. *Computer Program for Calculating and Fitting Thermodynamic Functions*; NASA Ref. Pub. 1271; NASA Lewis Research Center: Cleveland, OH, 1992.
(82) Georgievskii, Y.; Miller, J. A.; Burke, M. P.; Klippenstein, S. J. Reformulation and Solution of the Master Equation for Multiple-Well Chemical Reactions. *J. Phys. Chem. A* **2013**, *117*, 12146−12154.
(83) Available from authors on request.
(84) Jasper, A. W.; Miller, J. A. Lennard−Jones Parameters for Combustion and Chemical Kinetics Modeling from Full-Dimensional Intermolecular Potentials. *Combust. Flame* **2014**, *161*, 101−110.
(85) Troe, J. Theory of Thermal Unimolecular Reactions at Low Pressures. 1. Solutions of the Master Equation. *J. Chem. Phys.* **1977**, *66*, 4745−4757.
(86) Sivaramakrishnan, R.; Su, M.-C.; Michael, J. V.; Klippenstein, S. J.; Harding, L. B.; Ruscic, B. Rate Constants for the Thermal Decomposition of Ethanol and Its Bimolecular Reactions with OH and D: Reflected Shock Tube and Theoretical Studies. *J. Phys. Chem. A* **2010**, *114*, 9425−9439.
(87) Saxena, S.; Kiefer, J. H.; Klippenstein, S. J. A Shock Tube and Theory Study of the Dissociation of Acetone and Subsequent Recombination of Methyl Radicals. *Proc. Combust. Inst.* **2009**, *32*, 123−130.
(88) Jasper, A. W.; Oana, C. M.; Miller, J. A. "Third-body" Collision Efficiencies for Combustion Modeling: Hydrocarbons in Atomic and Diatomic Baths. *Proc. Combust. Inst.* **2015**, *35*, 197−204.
(89) Harding, L. B.; Klippenstein, S. J.; Jasper, A. W. Ab Initio Methods for Reactive Potential Surfaces. *Phys. Chem. Chem. Phys.* **2007**, *9*, 4055−4070.
(90) Jasper, A. W.; Miller, J. A. Theoretical Unimolecular Kinetics for $CH_4 + M \rightarrow CH_3 + H + M$ in Eight Baths, M = He, Ne, Ar, Kr, H_2, CO, N_2, and CH_4. *J. Phys. Chem. A* **2011**, *115*, 6438−6455.
(91) Albaladejo, J.; Jimenez, E.; Notario, A.; Cabanas, B.; Martinez, E. CH_3O Yield in the $CH_3 + O_3$ Reaction Using the LP/LIF Technique at Room Temperature. *J. Phys. Chem. A* **2002**, *106*, 2512−2519.
(92) Kukui, A.; Boustrot, V.; Laverdet, G.; Le Bras, G. Mechanism of the Reaction of CH_3SO with NO_2 in Relation to Atmospheric Oxidation of Dimethyl Sulfide: Experimental and Theoretical Study. *J. Phys. Chem. A* **2000**, *104*, 935−946.
(93) Wollenhaupt, M.; Crowley, J. N. Kinetic Studies of the Reactions $CH_3 + NO_2 \rightarrow$ Products, $CH_3O + NO_2 \rightarrow$ Products, and $OH + CH_3C(O)CH_3 \rightarrow CH_3C(O)OH + CH_3$, over a Range of Temperature and Pressure. *J. Phys. Chem. A* **2000**, *104*, 6429−6438.
(94) Glanzer, K.; Troe, J. Reactions of Alkyl Radicals in Shock Wave-Induced Pyrolysis of Nitroalkanes. *Ber. Bunsen-Ges. Phys. Chem.* **1974**, *78*, 182−184.
(95) Biggs, P.; Canosa-Mas, C. E.; Fracheboud, J. M.; Parr, A. D.; Shallcross, D. E.; Wayne, R. P.; Caralp, F. Investigation into the Pressure-Dependence Between 1 and 10 Torr of the Reactions of NO_2 with CH_3 and CH_3O. *J. Chem. Soc. Faraday Trans.* **1993**, *89*, 4163−4169.
(96) Yamada, F.; Slagle, I. R.; Gutman, D. Kinetics of the Reaction of Methyl Radicals with Nitrogen Dioxide. *Chem. Phys. Lett.* **1981**, *83*, 409−412.
(97) Su, M. C.; Kumaran, S. S.; Lim, K. P.; Michael, J. V.; Wagner, A. F.; Harding, L. B.; Fang, D. C. Rate Constants, $1100 \leq T \leq 2000$ K, for $H + NO_2 \rightarrow OH + NO$ Using Two Shock Tube Techniques: Comparison of Theory to Experiment. *J. Phys. Chem. A* **2002**, *106*, 8261−8270.
(98) Baulch, D. L.; Cobos, C. J.; Cox, R. A.; Esser, C.; Frank, P.; Just, T.; Kerr, J. A.; Pilling, M. J.; Troe, J. Evaluated Kinetic Data for Combustion Modeling. *J. Phys. Chem. Ref. Data* **1992**, *21*, 411−734.

DOI: 10.1021/acs.jpca.5b01563
J. Phys. Chem. A 2015, 119, 7872−7893